2020-01-01

Machine Learning Analysis to Characterize Phase Variations in Laser Propagation Through Deep Turbulence

Luis Fernando Rodriguez Sanchez

University of Texas at El Paso

Recommended Citation

Rodriguez Sanchez, Luis Fernando, "Machine Learning Analysis to Characterize Phase Variations in Laser Propagation Through Deep Turbulence" (2020). *Open Access Theses & Dissertations*. 3028.
https://scholarworks.utep.edu/open_etd/3028

MACHINE LEARNING ANALYSIS TO CHARACTERIZE PHASE VARIATIONS IN LASER PROPAGATION THROUGH DEEP TURBULENCE.

LUIS FERNANDO RODRIGUEZ SANCHEZ

Doctoral Program in Mechanical Engineering

APPROVED:

Vinod Kumar, Ph.D., Chair

V.S. Rao Gudimetla, Ph.D., Co-Chair

Arturo Bronson, Ph.D.

Heidi Taboada, Ph.D.

Jorge Munoz, Ph.D.

V M Krushnarao Kotteda, Ph.D.

Stephen L. Crites, Jr., Ph.D.
Dean of the Graduate School

Dedication

I dedicate this dissertation to my wife Marta and my children Luis Fernando and Marta for all their permanent support in the realization of this dream. To my mom Lupita, for her wisdom and continuous support, my sister Angélica, and her husband Konrad for their unconditional support at a time when my family really needed their help. To my brother David who has had a key role in the theory components of this dissertation and always has been my motivation to be his guide. To all my brothers and sisters. To all my in-laws for their unconditional support.

I also dedicate it to my dad Ricardo from whom I learned and inherited a taste for the Mechanical Engineering and the discipline for the study of the physical sciences.

Finally, I dedicate this dissertation to all my professors from whom I received a taste for the scientific knowledge.

MACHINE LEARNING ANALYSIS TO CHARACTERIZE PHASER VARIATIONS IN LASER PROPAGATION THROUGH DEEP TURBULENCE.

by

LUIS FERNANDO RODRIGUEZ SANCHEZ

DISSERTATION

Presented to the Faculty of the Graduate School of
The University of Texas at El Paso
in Partial Fulfillment
of the Requirements
for the Degree of

DOCTOR OF PHILOSOPHY

Department of Mechanical Engineering
THE UNIVERSITY OF TEXAS AT EL PASO
May 2020

Acknowledgements

This work is supported by Air Force Office of Scientific Research (AFOSR) under Grant Number BAA-AFRL-AFOSR-2016-0007, and Department of Mechanical Engineering at University of Texas at El Paso. Simulations were running on XSEDE computational resources such as Bridges, Stampede, and Lonestar. I would also like to thank Dr. Stacie Williams, AFOSR Program Officer, for her hard work that helped to provide the grant.

I would like to pay my special regards to Dr. Vinod Kumar, my advisor, for his continued guide and support in all this walk towards the end of my doctoral studies. To Dr. Heidi Taboada, who was the main contact and from whom I received a lot of support for my doctoral studies at UTEP. To her husband, Dr. José Espiritu from whom I received unconditional advice.

To Dr. Rao Gudimetla, my co-advisor, for his unconditional support and advice while carrying out this research. To Dr. Arturo Bronson, for his patience and support in making the necessary corrections to this work. To Dr. V.M. Kotteda, for his continued help on supercomputational issues. To Dr. Jorge Munoz, which guidance in the topic Neural Networks was crucial for giving shape to this dissertation. To Dr. Christopher Harris, for his enormous support correcting this dissertation.

To all my evaluation committee who has been the unconditional guide to shape this dissertation, as well as to give the proper focus to my research. To all the members of the Dr. Kumar research team whose unconditional support gave the right structure to this dissertation, particularly Arturo Rodriguez and Arturo Schiaffino.

To UTEP, which is without a doubt a top university, for allowing me to fulfill this dream. To Tec de Monterrey campus Monterrey because it opened the doors to me for starting my doctoral studies into that excellent institution.

To Dr. Nicolás Hendrichs and Dr. Alex Elías from Tec de Monterrey for their friendship and support on difficult moments. To Dr. Isaac Jimenez and Dr. Hector Siller, who represented an enormous initial impulse for the realization of my doctoral studies.

To Professors Nardo Hernández and Lucio Saldívar who gave me the solid foundations of Physics and Chemistry that I currently use. To Professors Víctor Medellín and Esthela Salado who gave me a strong training in Mathematics. To Professor Silvia Licón, who taught me the art of order and cleanliness in writing, accounting records, and financial planning.

To all my professors at UTEP and Tec de Monterrey who shaped my doctoral studies.

Abstract

The present dissertation is focused on the analysis of the atmospheric conditions of a turbulent environmental system and its effects on the diffraction of a laser beam that moves through it. The study is based on the optical communication of two labs placed at the summit of two mountains located in Maui, Hawaii. The emitter system is located at the Mauna Loa mountain and the receiver at the Haleakala. The distance between both mountains is 150 km. The emitter system is at a height of 3.1 km and the receiver at 3.4 km. The maritime environment at the location experiences continuous atmospheric of turbulence. The turbulence conditions present a series of rotating systems called Eddies, which act as a kind of lens that diffuses light because they change the refractive index of the air, affecting the phase of the laser beam used in the communication. Thus, the objective of this study has been to find a mathematical relation between the level of turbulence, measured by the Reynolds number, and an optical parameter, represented by the structure constant of refractive index C_n^2 for measuring the optical disturbance. The profile of temperatures is required to perform the calculations of the C_n^2. I lacked experimental data, so I used a CFD simulation software called ANSYS Fluent. Additionally, neural network algorithms were used to fit the temperature data to an equidistant coordinate network. At the end of the study, the positive correlation between Reynolds and C_n^2 was obtained and an equation that shows the positive trend between both parameters.

Executive Summary

The presence of strong turbulence in atmosphere along the laser propagation path affects the quality of laser-based remote sensing and imaging and presents challenges to remote sensing technologies. To improve the quality of image detection and target selection in presence of the turbulence there is a need for characterizing these conditions.

The goal is to develop new correlations to effectively characterize and compensate the images for turbulent effects. There is a location at Maui, Hawaii, where Air Force Research Laboratories (AFRL) communicate at the top of two mountains named Mauna Loa and Haleakala using optical devices. These laboratories are particularly interested in developing new metrics for deep turbulence effects on laser propagation through long path.

The approach to get these correlations was the Kolmogorov´s theory, which states that in turbulent media, kinetic energy is transferred through a series of rotational systems called Eddies that decrease in size as the kinetic energy is transferred.

Kolmogorov defined the behavior of velocity variations in a turbulent environment through the function of velocity structure. Since the objective was to find correlations that allowed characterizing the effects of turbulent flow on optical variables, the optical variable that was decided to study is the constant of the diffusion index C_n^2 that depends on the temperature variations.

C_n^2 depends on temperature variations. Such temperature variations follow a pattern similar to the velocity variations defined in the Kolmogorov´s structure function. For this reason, it was decided to use that relationship for the calculation of C_n^2.

The temperature data necessary to calculate the variations was obtained through a fluid simulation software called ANSYS Fluent, since it did not have experimental data. The information obtained from the software is not generated in equidistant coordinates as required to apply the equation. This is where the use of neural networks is necessary to generate that information.

Neural networks are algorithms that have the characteristic of being able to predict information based on data with which it has been previously trained. The algorithm used was trained with the spatial information obtained from the ANSYS Fluent and later fed with a profile of equidistant coordinates to predict the temperatures exactly in those coordinates.

These new series of data based on an equidistant mesh allowed me to use the equation to calculate the value of C_n^2. The next step was to relate these values to the level of turbulence present in each case.

The best way to define the level of turbulence is the Reynolds number, which is directly related to the wind velocity. The range of atmospheric velocities at the height of this region of Maui ranges from 5 to 16 m/s and I selected a time step of 0.25 m/s to generate the cases of study, where each velocity corresponded to one case. At the end I generated 45 cases.

For each of the 45 cases of velocity and Reynolds numbers, I carried out the same process of exporting the temperature profile from the ANSYS Fluent, adjusting the generated values with neural networks, and finally calculating the C_n^2 values.

In the end, a table and a graph were generated with the corresponding values between the Reynolds number and the constant of the structural function of temperature, finding a positive correlation between both variables and a linear trend equation.

Table of Contents

List of Tables

List of Figures

Chapter 1: Introduction.

Laser propagation through atmospheric turbulence has been of interest by many scientists and engineers for centuries. Before the invention of lasers, astronomers observed the light coming from the stars distorted by a turbulent atmosphere. After the invention of lasers, scientists and engineers observed similar phenomenon specially on long distances, then many focused their efforts on understand it, particularly after the appearance of optical communication systems [1].

The first intentional approach is the use of analytical equations to understand the turbulent behavior of the atmosphere. The Navier-Stokes equation is excellent due to the inclusion of all the variables involved in the fluid phenomena, the truly weakness of this approach is the enormous quantity of calculations that takes part in every case of analysis. Even though talking about high performance computer capacity, the volume of fluids that can be fully calculated using Navier-Stokes equations is very small [2].

Then, a different approach is used for analyzing the behavior of the turbulent atmosphere, which is the theory of the energy cascade of Kolmogorov. This approach defines that the energy from the turbulent atmosphere is transmitted inside a spam called inertial subrange [3].

On the other hand, counting on the CFD fluid simulation resource by ANSYS Fluent, we decided to use it to make important contributions to the understanding of the turbulent conditions in the analyzed volume of turbulent air between two mountains.

Due to the random approach of ANSYS for mesh construction and the importance for our study to have a proportional mesh with specific values of pressure, temperature and wind velocity, we decided to use another source for exporting that data but work the results to obtain a proportional matrix with the corresponding speed, pressure and temperature data within a proportional mesh.

This other resource is called neural networks, which are computational algorithms that estimate conditions based on a group of data used as training group. In the present case, the data corresponding to an atmospheric volume generated on a non-proportional mesh were used to train the algorithm and thereby estimate the temperature, pressure and speed conditions of another structured atmospheric volume based on a proportionate spatial mesh.

The need to have a proportional mesh is to calculate the optical parameter called diffraction constant C_n^2. The objective of the thesis is to find the relation between the Reynolds number and the values of C_n^2, and the values of C_n^2 are calculated on proportional deltas of distance, which accuracy would be enormously low basing the calculations on a non-proportional mesh [4].

At the end, the calculations of C_n^2 related to Reynolds number took us to the conclusion that there is a correlation of the Reynolds number over C_n^2 but only after velocities of 13 m/s that are present in the Hawaiian environment during the months of October through late January and May through July [2].

A future work is focused on relating data obtained from atmospheric devices to compare with the current analytical approach. The Dr. Rao, who belongs to the AFOSR laboratory at Maui, has validated these correlations as very close to the real turbulent behavior [1].

.

Chapter 2: Background and Literature Review.

This chapter shows the entire theoretical basis used for the development of this study. The first concepts are those based on the fundamental mathematics to understand the optical propagation, with a strong basis on the theories presented by Tatarskii [5].

The following concepts are related to the Kolmogorov's theory, which seeks to explain the turbulence phenomenon by means other than the Navier-Stokes equations and proposing its Energy Cascade Theory and the concept of rotational systems called Eddies. through which this energy is transferred. The Eddies are rotational systems through which the kinetic energy is transferred from a high level position with the largest Eddies sizes, until the complete dissipation of energy with Eddies sizes too small that the rest of the energy dissipates in the form of heat. These Eddies are the cause of laser diffraction since they act as atmospheric lenses.

Additionally, Kolmogorov proposes a mathematical model to link the turbulence model with fluctuations in refractivity, using the structural function of temperature and the power spectral density. This section is titled Turbulence Model of Refractivity Fluctuations. From this section the structural function of temperature was extracted, which was used for calculations of the structural constant of temperature C_T^2 and from it, the structural constant of the index of refractivity C_n^2.

After the Kolmogorov's analysis, I present a section related to observing the turbulent atmospheric effects on C_n^2 using the Fried parameter, which is based on statistical methods that relates to Gauss's theory. I linked this section with a presentation of the typical C_n^2 behavior on a summer day in Maui with a graph based on experimental readings, to have an example of what could be obtained with the present study.

Due to the enormous amount of data from the temperature readings and that were used in matrix form, the numerical methods are presented in this section as a tool to calculate the structural functions C_T^2 and C_n^2. On the other hand, they are also presented here because other members of Dr. Kumar's team, already have been working with relating the atmospheric turbulence and the optical variables. Particularly Diego Lozano used profusely used the numerical methods for generating phase screens that allowed him to see the laser's phase variation at intermediate positions on its path.

On the other hand, because I did not have access to experimental information of the temperature profiles, all the temperature profiles corresponding to each case of wind velocity were generated through a CFD simulation software called ANSYS Fluent. For this reason, I present a section explained in detail about the theoretical foundations behind the Fluid Dynamics and Computational Fluid Dynamics (CFD).

The profiles of temperature were generated to calculate the structural function of the temperature C_T^2, which in turn will allow the calculation of C_n^2. However, to apply the structural temperature equation, it is necessary to have a temperature profile defined in a series of equidistant coordinates, since the position vector must be constant between each coordinate. This condition of equidistant positions is not fully generated with the CFD simulation software.

To generate this temperature profile at equidistant coordinate positions, I used neural network algorithms. These algorithms can be trained with a series of data and then make predictions based on this training. The neural algorithms were trained with the information obtained from the CFD simulation; after this training, the algorithm was fed with a series of equidistant positions to make the predictions at each coordinate. For this reason, at the end of this chapter, a specific section is dedicated to explaining in detail the theoretical basis of the operation of neural network algorithms.

Fundamentals of Optical Propagation

The general description of our project starts with the theoretical bases of light propagation or more commonly known as optical propagation. It is worth remembering that a general accepted way to understand the propagation of light is to understand the light phenomena it as a wave of an electromagnetic nature. Then, for this reason, Maxwell's equations have a clear application [6].

During this chapter, theoretical results will be obtained from Maxwell's equations, using a perturbation technique described by Tatarskii [5]. For the sake of simplicity, a plane wave is assumed to be incident upon the random medium and just the resultant fluctuations of amplitude and phase are considered.

The Wave Equation for Optical Propagation. The atmosphere is assumed to have zero conductivity and unitary magnetic permeability, while the electromagnetic field is assumed to have a sinusoidal time dependence, given by $e^{-i\omega t}$. Amplitude and phase statistics for short pulses can be derived by Fourier decomposition of their waveform into a spectrum of plane waves [6]. Given such conditions, Maxwell's equations are written as follows:

$$\nabla \cdot H = 0 \tag{2.1}$$

$$\nabla \times E = ikH \tag{2.2}$$

$$\nabla \times H = -ikn^2 E \tag{2.3}$$

$$\nabla \cdot (n^2 E) = 0 \tag{2.4}$$

Where $i = \sqrt{-1}$, $k = \frac{\omega}{c}$ stands for the wave number of the radiation, ω for its radian frequency, and c is the speed of light in free space. The operator ∇ is the vector derivative $\left(\frac{\partial}{\partial x}, \frac{\partial}{\partial y}, \frac{\partial}{\partial z}\right)$. Both E and H correspond to the vector amplitudes of the electric and magnetic field, respectively, and are position dependent functions. The assumed sinusoidal time dependence is contained in k. Finally, $n(r)$ is the atmospheric refractive index in a position dependent random function [9].

The most commonly known wave equation for the electric field is obtained by substituting (2.3) in (2.2) as seen below:

$$-\nabla^2 E + \nabla(\nabla \cdot E) = k^2 n^2 E \qquad (2.5)$$

Then (2.4) is expanded and solved for $\nabla \cdot E$ and the result inserted into (2.5) to obtain:

$$\nabla^2 E + k^2 n^2 E + 2\nabla(E \cdot \nabla \log(n)) = 0 \qquad (2.6)$$

In (2.5), $2\nabla(E \cdot \nabla \log(n))$ refers to the change in polarization as the wave propagates, which is considered negligible for $\lambda \ll l_0$ [2]. Depolarization effects of the atmosphere are even negligible for $\lambda > l_0$. Thus, (2.6) can be rewritten as:

$$\nabla^2 E + k^2 n^2 E = 0 \qquad (2.7)$$

Finally, the desired results are obtained by solving equation (2.7).

Solution by the Method of Small Perturbations. The method consists of a series of decreasing E terms. As assumption, each E_m is of the order of smallness $(n_1)^m$. If $|E_{m+1}| \ll |E_m|$, then the series converge, and propagation is accurately described. Otherwise, the series would diverge. Physically, the order of the terms represents the scattering of the wave [7]. The zero-order for unscattered, first order for single scattering, and so on. For the current analysis, just the single scatter case is solved.

First, $E = E_0 + E_1$ is inserted into (2.7) and terms of the same order in n_1 are gathered and equated to zero, as follows:

$$\nabla^2 E_0 + k^2 E_0 = 0 \tag{2.8}$$

$$\nabla^2 E_1 + k^2 E_1 + 2k^2 n_1 E_0 = 0 \tag{2.9}$$

The product $E_1 n_1$ is of order n_1^2, therefore, it is ignored. As *Tataraskii* [13], the incident field is assumed to be a unit amplitude plane wave propagating in the z direction, $E_0 = e^{ikz}$, so (2.9) is rewritten as:

$$\nabla^2 E_1 + k^2 E_1 = -2k^2 n_1 e^{ikz} \tag{2.10}$$

Now, its solution is the convolution of the term on the right side with the Green's function of the equation:

$$E_1(r) = (4\pi)^{-1} \int_V d^3\, r e^{\frac{ik\left[(\varrho-\varrho')^2\right]}{2(z-z')}} \left[2k^2 n_1(r') e^{ikz'}\right] \tag{2.11}$$

It is stated that the scattered field observed in r is a spherical wave emitted at r', with an amplitude proportional to the product of the local refractive index $n_1(r')$ and the strength of the incident radiation.

The equation in (2.11) can be simplified by the characteristics of laser propagation: Monochromatic, scattered by weak large-scale refractivity fluctuations and contained in a narrow cone in the forward scatter direction $(+z)$. From laws of diffraction, the maximum scattering angle is in the smallest eddies traversed. In this case, the scattering angle $\frac{\lambda}{l_0}$ is 3×10^{-4} radians, therefore, the transverse displacement from the forward propagation from scatterer to receiver $|\varrho - \varrho'|$ is much smaller than the distance between them $|z - z'|$. That is, if $|z - z'| \gg |\varrho - \varrho'|$, then $r - r'$ can be replaced by $z - z'$ in the denominator of (2.11). For the argument, the wavelengths that are contained within this distance must be considered. Thus, the terms that are retained are the ones that make the argument larger than 2π radians [1]. Then, $|r - r'|$ is expanded into a binomial series, and after reducing it by the Fresnel approximation, the following equation is obtained:

$$E_1(r) = \frac{k^2 e^{ikz}}{2\pi} \int_V d^3 r' e^{\frac{ik\left[(\varrho-\varrho')^2\right]}{2(z-z')}} \frac{n_1(r')}{(z - z')} \tag{2.12}$$

This equation is the Fresnel diffraction formula and is the solution to the diffusion equation when the source term is $-2k^2 n_2$. Now, in order to calculate how the amplitude and phase fluctuate when crossing the atmosphere relatively to the free space, the field E is rewritten as:

$$\frac{E}{E_0} = \frac{k^2 e^{ikz}}{2\pi} \int_V d^3 r' e^{\frac{ik\left[(\varrho-\varrho')^2\right]}{2(z-z')}} \frac{n_1(r')}{(z-z')} \tag{2.13}$$

This is the Fresnel diffraction formula and is the solution to the diffusion equation when the source term is $-2k^2 n_2$. In addition, the exponential term predicts the location of the interference fringes produced in the receiving plane in z by the interference of the incident plane wave and the scattered spherical wave (Huygen's wavelet) emitted from (ϱ', z').

Now, to calculate how amplitude and phase fluctuate when crossing the atmosphere relatively to the free space [11], the field $E = E_0 + E_1$ must be written in terms of both amplitude and phase as follows:

$$\frac{E}{E_0} = 1 + \frac{E_1}{E_0} = \frac{A}{A_0} e^{i(s-s_0)} \tag{2.14}$$

The last term results from $E = Ae^{is}$ and $E_0 = A_0 e^{is_0}$, where A_1 is the amplitude of E_1. Then, its natural logarithm is taken. Since $\left|\frac{E_1}{E_0}\right| \ll 1$ and $\frac{A_1}{A_0} \ll 1$, the logarithm is expanded into a power series and just the first term is retained, as follows:

$$\frac{E_1}{E_0} \cong \frac{A_1}{A_0} + i(s - s_0) \tag{2.15}$$

Equation (2.15) implies that, when normalized by E_0, amplitude ratio and phase fluctuations must be obtained from (2.12), from its real and imaginary parts, respectively [12]. Resulting in:

$$\frac{A_1}{A_0} = \frac{k^2}{2\pi}\int_V d^3\, r' \cos\left[\frac{k(\varrho-\varrho')^2}{2(z-z')}\right]\frac{n_1(r')}{(z-z')} \qquad (2.16)$$

$$(s-s_0) = \frac{k^2}{2\pi}\int_V d^3\, r' \sin\left[\frac{k(\varrho-\varrho')^2}{2(z-z')}\right]\frac{n_1(r')}{(z-z')} \qquad (2.17)$$

Where there is no wave attenuation as $n_1(r')$ is real. Now, log amplitude $\chi = \ln\left(\frac{A_1}{A_0}\right) \cong \frac{A_1}{A_0}$ (what is often measured experimentally) and $s - s_0 = s_1$ are defined by convention. It should be noted, though, that χ is identical to $\frac{A_1}{A_0}$ for weak scatterings as in the current case. Furthermore, as the analysis is considering a plane wave, statistical homogeneity of both amplitude and phase is expected to remain constant in the plane z [8]. On the other hand, χ and s are expected to fluctuate along the z axis (in the propagation direction), with a growth directly proportional to the distance travelled as it propagates through more refractive turbulence. Consequently, $n_1(r')$ is expanded into a two-dimensional Furier-Stieltjes transform as follows:

$$n_1(r') = \int d\nu(K, z')\, e^{iK\cdot\varrho'} \qquad (2.18)$$

Where the variation of $n_1(r')$ is transformed only in the plane transversal to the propagation direction and $d\nu$ is set as function of z'.Then, equation (2.17) is inserted into (2.15) and (2.16), and integration over $d\nu$ is substituted with that over d^3r' (since $d^3r' = d^2\varrho' dz'$) to obtain:

$$\begin{bmatrix}\chi(r)\\ s_1(r)\end{bmatrix} = \frac{k^2}{2\pi}\int\int_0^z dz'\int d^2\varrho' e^{iK\cdot\varrho'}\begin{Bmatrix}\cos\\ \sin\end{Bmatrix}\left[\frac{k(\varrho-\varrho')^2}{2(z-z')}\right] \tag{2.19}$$

The integral over ϱ' is performed after substituting $\varrho'' = \varrho' - \varrho$. Now, since the sine and cosine terms are function of $|\varrho''|$, polar coordinates $\varrho'' = (\varrho'', \theta)$ can be used to integrate directly over θ. Additionally, the inner integrals are rewritten in terms of $I_{1,2}$, as follows:

$$I_{1,2} = e^{iK\cdot\varrho}\int_0^\infty d\varrho''\varrho''\begin{Bmatrix}\cos\\ \sin\end{Bmatrix}\left[\frac{k\varrho''^2}{2(z-z')}\right]\int_0^{2\pi} d\theta e^{iK\varrho''\cos(\theta-\psi)} \tag{2.20}$$

Where $K = (K, \psi)$ is let in the last term. The solution of the inner integration is the Bessel function $2\pi J_0(K\varrho'')$, which is then substituted in (2.20):

$$I_{1,2} = 2\pi e^{iK\cdot\varrho}\int_0^\infty d\varrho''\varrho'' J_0(K\varrho'')\begin{Bmatrix}\cos\\ \sin\end{Bmatrix}\left[\frac{k\varrho''^2}{2(z-z')}\right] \tag{2.21}$$

The remaining integral is the Hankel transform of the trigonometric term, which, when solved, (2.20) becomes:

$$I_{1,2} = \frac{2\pi(z-z')}{k}e^{iK\cdot\varrho}\begin{Bmatrix}\sin\\ \cos\end{Bmatrix}\left[\frac{k\varrho''^2}{2(z-z')}\right] \tag{2.22}$$

The resulting expression is then inserted into (2.19) to obtain:

$$\begin{bmatrix}\chi(r)\\ s_1(r)\end{bmatrix} = \int e^{iK\cdot\varrho}\left(k\int_0^z dz' d\nu(K,z')\begin{Bmatrix}\sin\\ \cos\end{Bmatrix}\left[\frac{K^2(z-z')}{2k}\right]\right) \tag{2.23}$$

This equation is interpreted as a two-dimensional Fourier expansion as (2.18). Therefore, the terms in brackets represent the random spectral amplitudes of both amplitude and phase fluctuations [9].

As in any random process, the properties of the outcome of experiments were averaged. Consequently, the two-dimensional covariance functions $B_\chi(\varrho)$ and $B_s(\varrho)$ are used to settle the statistical homogeneity of amplitude and phase in the plane z = constant. (It should be noted that $\langle\chi\rangle = \langle s_1\rangle = 0$ since $\langle n_1\rangle = 0$ by definition and because only the first order term $E_1$was retained.) Now, since both functions are often computed in the receiving plane located at $z = L$, they're defined as $B_\chi(\varrho, z) = \langle\chi(\varrho_1 + \varrho, z)\chi * (\varrho_1 + z)\rangle$ and $B_s(\varrho, z) = \langle s(\varrho_1 + \varrho, z)s * (\varrho_1 + z)\rangle$. Then, (2.23) is rewritten as:

$$\begin{bmatrix} B_\chi(\varrho) \\ B_s(\varrho) \end{bmatrix} = k^2 \int\int e^{iK\cdot(\varrho_1+\varrho)-iK'\cdot\varrho_1} \int_0^z dz' \int_0^z dz'' \left\{ \begin{matrix} \sin \\ \cos \end{matrix} \left[\frac{K^2(z-z')}{2k}\right] \begin{matrix} \sin \\ \cos \end{matrix} \left[\frac{K'^2(z-z'')}{2k}\right] \right\} \cdot \langle dv(K, z')dv * (K', z'')\rangle \tag{2.24}$$

Furthermore, the equation for the two-dimensional random amplitude dv is:

$$\langle dv(K, z')dv * (K', z'')\rangle = \delta(K - K')F_n(K', z' - z'')d^2Kd^2K'' \tag{2.25}$$

Where $F_n(K', z' - z'')$ is the two-dimensional spectral density of $n_1(r')$, defined by:

$$F_n(K', z' - z'') = \int_{-\infty}^{\infty} dK_z\, \phi_n(K', K_z)\cos[K_z(z' - z'')] \tag{2.26}$$

The ϕ_n term is the three-dimensional refractivity spectrum. Then, (2.24) is inserted into (2.23), where the K' integration is performed to obtain:

$$\begin{bmatrix} B_\chi(\varrho) \\ B_s(\varrho) \end{bmatrix} = \int d^2K e^{iK\cdot\varrho}$$

$$\cdot\left(k^2\int_0^z dz'\int_0^z dz'' \begin{Bmatrix} \sin \\ \cos \end{Bmatrix} \left[\frac{K^2(z-z')}{2k}\right] \begin{matrix} \sin \\ \cos \end{matrix} \left[\frac{K'^2(z-z'')}{2k}\right]\right\} F_n(K, z'-z'')\right) \tag{2.27}$$

The terms in brackets correspond to the two-dimensional spectral densities of χ and s, as demonstrated by their Fourier transform, which are then rewritten as $F_\chi(K,0)$ and $F_s(K,0)$.

Consequently, (2.27) is simplified in three phases [15]. First, it is noted from (2.26) that $F_n(K,z'-z'') = F_n(K,z''-z')$. Second, since F_n correlates n_1 along adjacent planes along the z axis, only homogeneities whose size $2\pi K^{-1} \geq |z'-z''|$ provide significant contributions. Therefore, F_n is expected to decay sharply for $K|z'-z''| > 1$. Then, (2.27) is rewritten as:

$$\begin{bmatrix} F_\chi(K,0) \\ F_s(K,0) \end{bmatrix} = k^2 \int_0^L d\xi\, F_n(K,\xi) \int_{\frac{\xi}{2}}^{L-\frac{\xi}{2}} d\eta \left[\cos\left(\frac{K^2\xi}{2k}\right) \mp \cos\left(\frac{K^2(L-\eta)}{k}\right)\right] \tag{2.28}$$

Where $L = z$ and the transformation of variables $\xi = z' - z''$, $2\eta = z' + z''$ is carried out. Finally, since $F_n \to 0$ for $\xi > K^{-1}$ and $K_{max} \sim 2\pi l_0^{-1}$ (where l_0 is the microscale of the turbulence), the argument of $\cos\left(\frac{K^2\xi}{2k}\right)$ satisfies $\frac{K^2\xi}{2k} \leq \frac{K}{2k}$, and $\frac{K}{2k} \ll 1$, respectively. Therefore, $\cos\left(\frac{K^2\xi}{2k}\right) \sim 1$ for entire integration over ξ. Furthermore, by assuming $\xi \ll L$, its presence can be ignored within the η integration limits, as K^{-1} has a maximum value of $\frac{L_0}{2\pi}$ (thus, $\xi \leq L_0$) for the Kolmogorov spectrum and region of integration $\xi \leq K^{-1}$. Lastly, if $L_0 \ll L$ then the ξ dependence is completely inserted into the η integral. This implies that the path must be much longer than the outer scale, which is satisfied when $L_0 \sim 1\ m$, near the ground [10]. Consequently, both integrals in (2.27) become independent and two expressions are obtained:

$$\int_0^\infty d\xi\, F_n(K,\xi) = \pi\phi_n(0,K) \tag{2.29}$$

Where the upper limit is replaced by infinity with negligible error, since $\xi \leq L_0$.

$$\begin{bmatrix} F_\chi(K,0) \\ F_s(K,0) \end{bmatrix} = \pi k^2 L \left[1 \mp \left(\frac{k}{K^2 L}\right) \sin\left(\frac{K^2 L}{k}\right)\right] \phi_n(K) \tag{2.30}$$

The Kolmogorov´s Theory.

The turbulence in the Earth's atmosphere is directly related to random variations in temperature and convective air movement, which alters the refractivity index of the air, both in position and in time. As optical waves propagate through the turbulent air, these waves are distorted by fluctuations in the refractive index of the atmosphere [11].

The equation of the refractive index of air referred to the optical frequencies is presented in equation (3.1). This equation will later be related to the turbulence equation to model its effects [11].

$$n - 1 = 77.6(1 + 7.52\ \times\ 10^{-3}\lambda^{-2})(P/T)10^{-6} \tag{2.31}$$

In this equation, P represents pressure in millibars, T represents temperature in K degrees, and λ is the wavelength of light in μm (micrometers). Then, n - 1 is closely related to the deviation of the refractivity index. The typical value at sea level is 3 x 10^{-4}.

The present study is focused on analyzing the simulation of the temperature changes and analyzing their effects in the refractive index to lay the foundations for future mathematical modeling that will allow us to overcome these effects [12].

To perform the simulation of the phenomenon of turbulence, one approach is the analytical use of the Navier-Stokes equations, however, as mentioned in the introduction, the volume of equations and operations required to solve the model is enormous; due to its size, other calculation tools were sought. Even so, the model is the basis of the CFD (Computational Fluid Dynamics) simulations used in this study to generate temperatures, pressures and velocities all over the volume under analysis [13].

In this way, our analysis was based on an approach that demands less amount of information and can help us to understand the phenomenon of turbulence through the Theory of Energy Cascade, proposed by the Russian mathematician Andrey N. Kolmogorov. For this reason, it is known as the Kolmogorov´s model [14].

Kolmogorov's idea is that when the kinetic energy enters a fluidic system, it does so through rotational systems called eddies. These eddies can be identified through their bigger diameters that are also called outer scale lengths, identified by L_o. whose size is larger when the process of transmitting kinetic energy starts into the system begins. Once the energy enters the major size eddies, it dissipates into smaller rotational systems until those systems reach the smallest diameters known as inner scale lengths or l_o. The Reynolds number corresponding to the eddies is $Re_o = u_o l_o$ [15].

After the eddies have reached their minimum size or the inner scale length, the rest of the kinetic energy dissipates as heat. All this phenomenon must occur within a range called inertial subrange, and Figure 2.1 shows how this dissipation occurs [16].

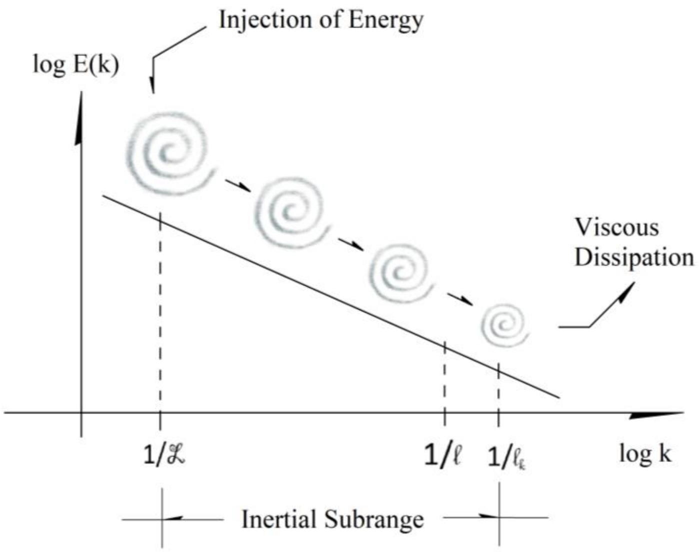

Figure 2.1: The Kolmogorov model of the energy cascade.

Figure 2.1 shows a turbulent system where the different sizes of eddies can be observed depending on the degree of kinetic energy dissipation.

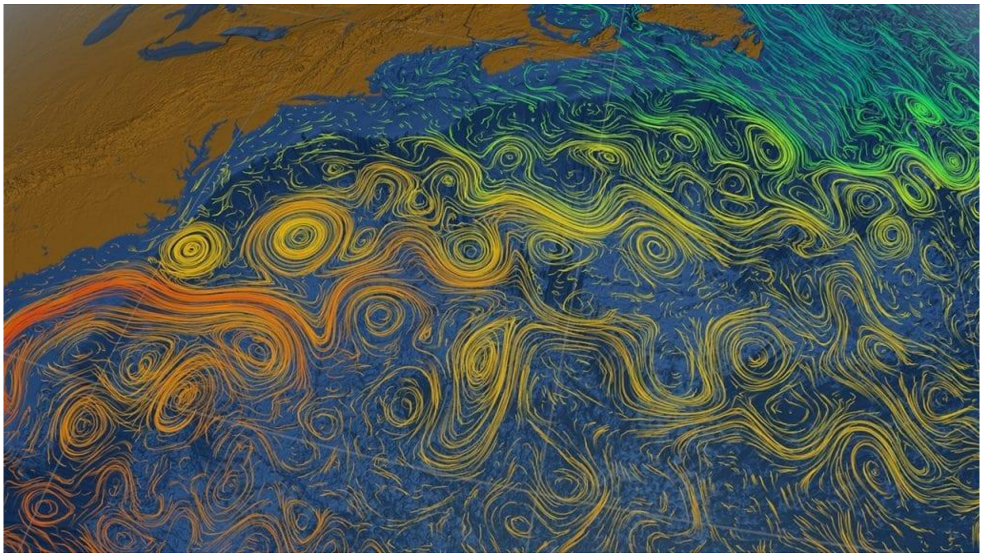

Figure 2.2: Rotational systems in turbulent media called eddies.

Structure Tensor. Based on the presence of the eddies in the turbulent environment, Kolmogorov proposes the structural equation of velocity.

The idea is to consider the velocities of two different points in the space which distance is defined by the vector ***r*** [17]. He has found that the mean-square velocity of the velocity difference could be described by a form called structure-function, which is defined as:

$$D_{ij}(r) = \langle [v_i(r_1 + r) - v_i(r_1)][v_j(r_1 + r) - v_j(r_1)] \rangle \qquad (2.32)$$

The structure equation in this case is referred to velocities in the different components. Important assumptions of homogeneity and isotropy are necessary to make this equation valid. The homogeneity establishes that the difference in velocity is only related to the displacement vector *r* [18] . The isotropy of the magnitude *r* is the most important concept.

The previous assumptions lead to the description of the turbulence as a single structure-function D_{rr}, thus, the following equation can describe it:

$$D_{rr} = \langle [v_r(r_1 + r) - v_r(r_1)]^2 \rangle \qquad (2.33)$$

Considering that *r* is within the inertial subrange, thus D_{rr} has the universal form

$$D_{rr} = {C_v}^2 r^{2/3} \qquad l_o < r < L_o \qquad (2.34)$$

C_v^2 is the structural constant of velocity, which has a direct relationship to the total amount of energy in the turbulent flow [19]. As mentioned above, this equation holds for the values of *r* that lie at the microscale level l_o to the outer turbulence scale L_o.

The microscale l_o corresponds to the lowest eddies size values in the limit of energy dissipation through viscosity effects. The outer scale L_o corresponds to the largest size of the scale for which the eddies can be considered isotropic. Near the ground the l_o has an order of size of millimeters while L_o has an order of meters. Both amounts show an increase with height at floor level [20].

Turbulence Model of Refractivity Fluctuations

The crucial point is to relate the turbulent model that Kolmogorov proposes to the refractivity equation. A key concept to establish this relation is the conservative passive additive defined by Professor Valerian Tatarskii [21]. Conservative quantities are the ones related to an identified air parcel and that parcel will keep the changes referred to those quantities no matter how much the parcel moves into space.

This is the reason why the way of analyzing temperature, pressure and speed must be based on the fluctuations of these properties. Because the variations in these properties follow a pattern similar to the variation in the velocity that was previously demonstrated through the velocity tensor, therefore the variations in temperature can be expressed using the structural constant of thermal variation.

$$D_T = {C_T}^2 r^{2/3} \tag{2.35}$$

Additionally, because refractivity has also a direct relationship with the velocity variations, the structural refractivity constant can as well be expressed using the same structural relation.

$$D_n = {C_n}^2 r^{2/3} = 8\pi \int_0^\infty k^2\, \Phi_n(k) \left[1 - \frac{sin(kr)}{kr}\right] dk \tag{2.36}$$

The previous relationship established with the concept of structural refractivity constant and the power spectral density of Kolmogorov (Φ), it is possible to determine the complete function of the power spectral density. This function can be calculated by inverting the previous equation in and solving it for the variable.

$$\Phi(k) = \frac{1}{4\pi^2 k^2} \int_0^{\infty} \frac{\sin(kr)}{kr} \frac{d}{dr} \left[r^2 \frac{d}{dr} D_n(r) \right] dr \tag{2.37}$$

k is the angular frequency measured in rad/m and is equal to $2\pi/\lambda$. Then, working with the previous equations, the following function can be obtained. This equation is valid in the Kolmogorov's inertial subrange [21].

$$\Phi_n(k) = 0.033\, {C_n}^2\, k^{-11/3} \qquad \frac{2\pi}{L_o} < k < \frac{2\pi}{l_o} \tag{2.38}$$

The power spectral density is the probability function associated with atmospheric turbulence. It is important to comment that there are turbulent atmospheric observations that deviate from the Kolmogorov's model, so it has also been necessary to find a statistical model that more accurately represents the effects of atmospheric turbulence [22].

Finally, relating the structural equations for the constants of temperature and refractivity, we have the final equation for the structural constant of refractivity as a function of pressure, temperature and the structural constant of thermal variation [23].

$${C_n}^2 = \left(\frac{79\, P}{T^2} \times 10^{-6} \right)^2 {C_T}^2 \tag{2.39}$$

The variations in temperature and pressure, as well as the structural variable of the temperature, were used to perform the calculations of the structural constant of refractivity for the present project.

Effects of Turbulence on Optical Propagation

Changes in the refractive index due to fluctuations in temperature are regularly smooth random functions of space and time. An auxiliary figure to understand the effects of variations in the refractive index is interpreting the presence of rotational systems or eddies as lenses [24].

In this model, the atmosphere could be assumed as a large number of random lenses with different shapes and sizes that move randomly into space. Figure 2.3 shows this phenomenon where the laser beam that leaves the emitting device, finds the different eddies that act as lenses and thus suffers variation in the direction due to different diffraction indices along the path, until it reaches the detector device [25].

Figure 2.3: Changes in laser direction due to the presence of eddies.

In the previous sections, the induced atmospheric effects on the refractive index were already characterized. In this section, we will observe the propagation of light as a flat wave front that moves through turbulent flow. The phase change is produced by changes in the refractive index of an atmospheric layer of thickness δh and height h as shown in the following equation [26]:

$$\varphi(x) = k \int_{h}^{h+\delta h} dz\, n(x,z) \tag{2.40}$$

The phase change can be affected by different variables in addition to the refractive index, for example layers that are thicker than the turbulent cell [27]. This is the reason why Gaussian statistics are used to estimate the phase changes, given the statistical properties of the refractive index.

Therefore, we can start this analysis by deriving the statistical data to show trends and patterns of behavior of a wave front.

$$U = e^{i\omega(x)} \tag{2.41}$$

The coherence function $B_h(\rho)$ needs to be denoted in terms of phase structure function with the purpose of doing this [25].

$$B_h(r) = \langle U(x)U^*(x+r)\rangle \tag{2.42}$$

$$Bh(r) = \langle e^{(i[\varphi(x) - \varphi(x+r)])}\rangle \tag{2.43}$$

Due to the Gaussian behavior of $[\varphi(x) - \varphi(x+r)]$, then the following relationship can be applied

$$\langle e^{(\alpha\chi)}\rangle = e^{\left(\frac{1}{2}\alpha^2\langle\chi^2\rangle\right)} \tag{2.44}$$

Therefore, the following equations can be derived [10]:

$$B_h(\rho) = e^{\left[-\frac{1}{2}\langle|\varphi(x) - \varphi(x+r)|^2\rangle\right]} \tag{2.45}$$

$$B_h(\rho) = e^{\left[-\frac{1}{2}D_\varphi(r)\right]} \tag{2.46}$$

Due to the chaotic behavior of the turbulent atmosphere, the stochastic processes such as velocity or temperature cannot be approximated as stationary. In any case, these stochastic processes can still be analyzed statistically if they have stationary increases [28]. Instead of focusing on the stochastic process based on time or a point in space $x(r)$, we center the analysis on the function $x(r + r_1) - x(r_1)$, that has a behavior close to stationary. The coherence function and the structure function can be simplified using the Fried Parameter.

$$B_h(\rho) = exp\left[-3.44\left(\frac{\rho}{r_o}\right)^{5/3}\right] \quad , \quad D_\varphi(\rho) = 6.88\left(\frac{\rho}{r_o}\right)^{5/3} \tag{2.47}$$

The coherence function and the phase structure function depend on the Fried Parameter [24], which is a function of the intensity of the turbulence, the zenith angle and the wavelength. This parameter will be widely used in characterizing the effects of atmospheric turbulence on the phase changes of the laser propagating into that medium.

Behavior of the Refractive Index C_n^2 in Open Atmosphere

Although the concept of refractivity index was previously referred to, with this chapter the purpose is to delve a little deeper into the concept commenting on important references about the behavior of it in the Earth's atmosphere depending on the time of day, the time of year and the height of the measurement [17].

As mentioned previously, the purpose of this analysis is to calculate the variability of the optical parameter denominated refractive index constant C_n^2 relative to Reynolds number. C_n^2 is the refractive index structure constant and is calculated in the equation (3.9).

The C_n^2 is dependent on the altitude and of the time in the day. Figure 2.4 shows a variation of the constant C_n in a lapse of 24 hrs. It can be observed from a range of 0.15×10^{-6} that happens where the sun is more brilliant to 1×10^{-6} particularly during the night [19].

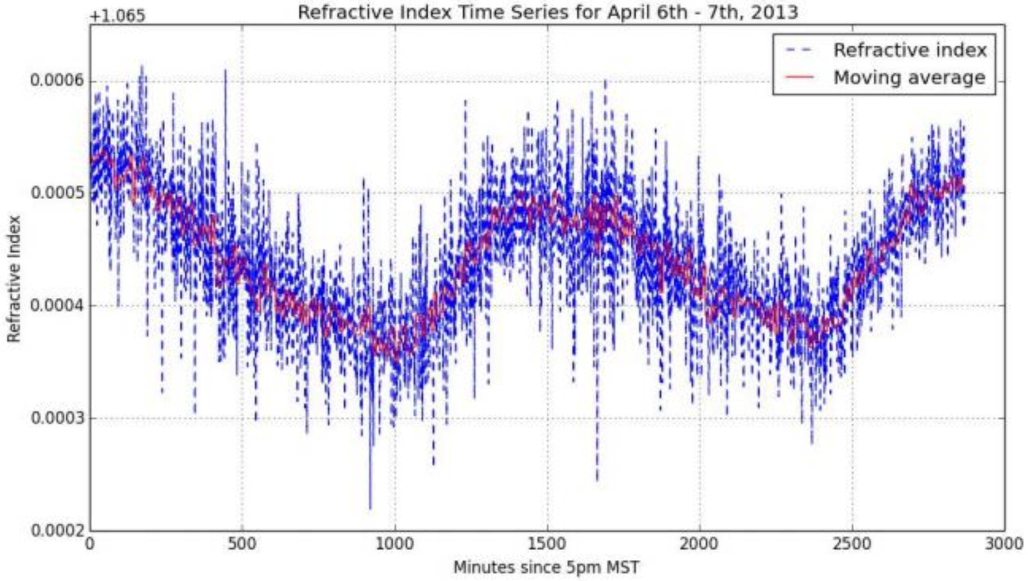

Figure 2.4: Distribution of the C_n value during a typical spring day in Hawaii.

The cycle of C_n during the day, represents a similar behavior on the surface of the earth (in the approximate range between 30 to 100 m). The fluctuation of temperatures, and therefore of C_n, is very reduced at night and the first hours of the morning. After the sun heats the soil, the process of atmospheric convection starts and, consequently, the temperature variations.

The instability due to convection generates temperature variations [29]. The process by which these temperature variations occur starts when the materials are heated by the sun. Then the air in contact with these surfaces heats up, loses density, and rises, colliding with the cold layers in its path and this mixture of layers of cold and hot air causes irregularities in the temperature. The heating process as the atmosphere irregularities continue during the day, which in turn causes an increase in C_n, until the end of the afternoon, when the solar heat falls [30] . Consequently, C_n values also decrease.

Typical C_n^2 values on a sunny day at the height of 2 m above the ground, are within a range of 10^{-17} $m^{-2/3}$ to 10^{-12} $m^{-2/3}$. Some other variations in the previous figure have to do with the sudden presence of clouds when the solar heat falls; consequently, the C_n values also decrease, since the grown quickly cools down and the structure of the temperature in the air becomes uniform rapidly [19].

Numerical Simulation of Laser Propagation.

The laser can be understood as an electromagnetic wave that suffers distortion in turbulent environment by the rotational phenomenon mentioned previously and that is called eddies. This distortion can be understood based on the theory of geometrical optics. The effect of the eddies in the optical waves, as also mentioned previously, is similar to thin lenses that can modify their waves [31].

During the current work, the simulation was done to measure the phase variance of a laser beam that propagates along horizontal paths in a maritime atmosphere between the top of two mountains where two important sites are placed, the Mauna Loa NOAA observatory and the AFRL AEOS telescope on Haleakala in Hawaii. The distance between them is 150 km and the height of the mountain, where the laser emitter is placed, is 3.1 km. On the other hand, the height of the mountain of the Haleakala, where the receptor is placed, is 3.4 km.

The equations to be modeled and solved through numerical methods have to be created in a geometric structure using a series of planes generated in a Cartesian system, in such a way that the entire laser path, as well as its phase changes can be understood plane by plane. Then the laser path is placed at the z coordinate, the vertical axis is y and the depth is x. The distance between the mountains is defined over the z axis and the height of the mountains is defined over the y axis [32].

Figure 2.5 represents the way in which the Cartesian axes were established on the volume under study. It is important to mention the definition of *observation plane* and *source plane* into the diagram. The source plane is represented by the emission point of the laser beam. The observation plane is placed in certain position along the z-axis where I have decided to perform the analysis of velocity, pressure and temperature as well as refractivity conditions.

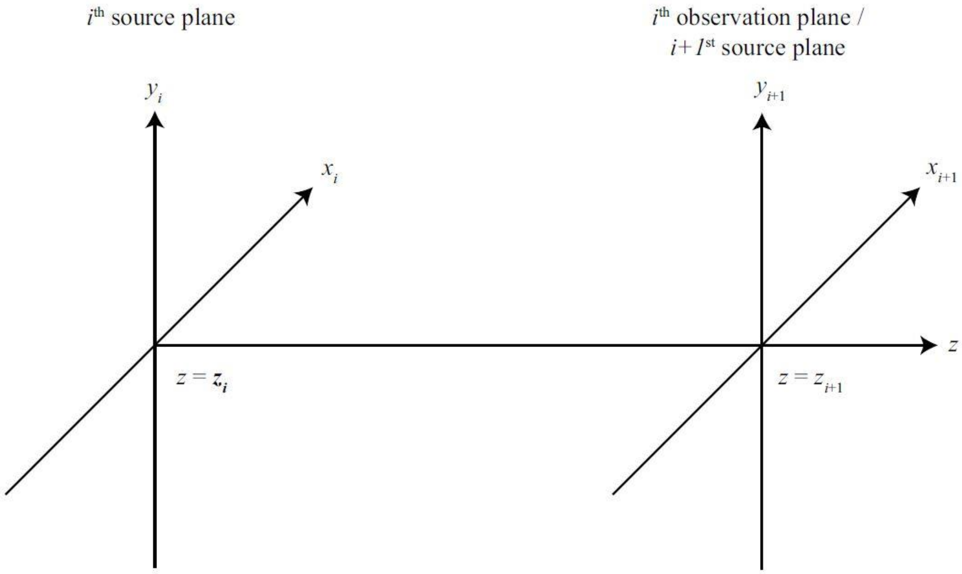

Figure 2.5: Definition of the source plane and observation plan inside a cartesian system

The geometry used in the figure establishes $r_1 = (x_1, y_1)$ the coordinates for the plane of the source and $r_2 = (x_2, y_2)$ for the plane of observation or receiver. The distance between the two planes is Δz. The figure shows the basic problem, given the optical plane of the source field $U(x_1, y_1)$, is necessary to define the field of the observation plane $U(x_2, y_2)$. The solution is found in the fraction integral given by Fresnel in the following equation [33]:

$$U(x_2, y_2) = \frac{e^{ik\Delta z}}{i\lambda\Delta z} \int_{-\infty}^{\infty} \int_{-\infty}^{\infty} U(x_1, y_1) e^{i\frac{k}{2\Delta z}[(x_1-x_2)^2 + (y_1-y_2)^2]} dx_1 dy_1 \tag{2.48}$$

In order to make a better observation of the laser phase behavior along the route, it is necessary to generate a certain number of planes, then the diagram shows an i^{th} observation plan. In this way, the z-axis has been divided by several planes to establish points of observation. Then each plane represents partial states of observation that allow the calculation of the atmospheric conditions such as velocity, temperature and pressure, based on previous results to finally calculate the diffractive index structure constant C_n^2 on each case [34].

In addition, a very powerful tool to analyze the behavior of laser diffraction is through the generation of phase screens. In the previous paragraph, there is a mention that the generation of intermediate planes allows the calculating of C_n^2, so it is worth mentioning also that it is possible to generate phase screens [35]. The phase screens are 2D maps, as seen in Figure 2.6, that through colors demonstrate the conditions of the laser phase and allow them to observe its behavior along the path.

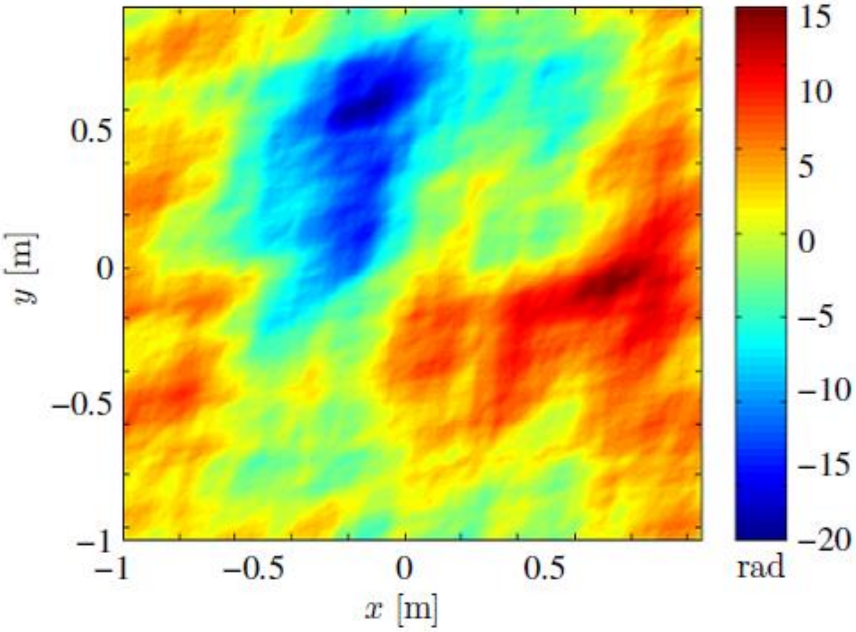

Figure 2.6: Distribution of the laser phase screen in a 2D map.

Fourier Transforms: from Analytical to Numerical. To solve the Fresnel equation using numerical methods, an important tool is the Fourier transform, since linear analysis and Fourier are essential tools for studying wave optics. Fourier spatial function g (s) and its inverse [36] are shown in the equation (2.49):

$$G(f_x) = \mathcal{F}\{g(x)\} = \int_{-\infty}^{\infty} g(x)e^{-i2\pi f_x x}dx \tag{2.49}$$

The first step to perform the conversion to numerical analysis is the discretization of the Fourier transform into a Riemann sum:

$$G(f_{xm}) = \mathcal{F}\{g(x_n)\} \tag{2.50}$$

$$G(f_x) = \sum_{n=-\infty}^{\infty} g(x_n)e^{-i2\pi f_{xm}x_n}(x_{n+1} - x_n)\ , \quad m = -\infty, \dots ,\infty \tag{2.51}$$

where *n* and *m* are integers. Computational calculations can only work with a finite number of samples N, so we set a δ interval such that $x_n = n\delta$ [37]. Then, the frequency of the interval is $\delta_f = 1/(N\delta)$ so that $f_{xm} = m\delta_f = m/(N\delta)$.

$$G\left(\frac{m}{N\delta}\right) = \mathcal{F}\{g(n\delta)\} \tag{2.52}$$

$$G\left(\frac{m}{N\delta}\right) = \delta \sum_{n=-N/2}^{N/2-1} g(n\delta)e^{-i2\pi mn/N}, \qquad n = -N/2, 1 - N/2, \dots, N/2 - 1 \tag{2.53}$$

The use of positive indices in the rearrangement of samples is similar to what occurs in the Discrete Fourier Transform [34]. The equation (2.54) shows the result:

$$g_{n'} = \frac{1}{N\delta} \sum_{m'=1}^{N} G_{m'} e^{i2\pi(m'-1)(n'-1)/N}, \qquad n' = 1, 2, \ldots, N \qquad (2.54)$$

The use of the discretization of the optical waves of the laser using the Fourier transform allowed us to apply numerical methods to predict the phase changes of the laser that were experiencing while propagating in turbulent media [31].

Fundamentals of Computational Fluid Dynamics.

As commented from the beginning of this work, the medium in which the laser beam is moving is experiencing turbulence due to the conditions of velocity, temperature and pressure. One of the most accurate ways to understand the fluidic phenomenon is through the equations of Louis Navier and George Gabriel Stokes. These scientists set out to describe the motion of viscous fluids by applying Newton's second law to motion fluids and assuming that the stress in the fluids is the result of a sum of diffuse viscosity and pressure [13].

These numerical relations are called Navier-Stokes equations, which are based on the assumption of an incompressible fluid with ρ and μ uniform and $\nabla \cdot U = 0$ [30]:

$$\rho \frac{DU_j}{Dt} = \mu \frac{\partial^2 U_j}{\partial x_i \partial x_i} - \frac{\partial P}{\partial x_j} - \rho \frac{\partial \Psi}{\partial x_j} \qquad (2.55)$$

The Reynolds number, $Re = uL/v$, is the unique free parameter if the forces are not present. In the case of our study, where we focus our research on a turbulent atmosphere, the value of the Reynolds number in the 10^6 units.

The typical wind velocities in Maui, where this study is based on, are within the range of 5 to 6 m/s, and since the average height of the mountains of 3250 m, and with a laser dispersion range of 3 m that takes part of the characteristic, the Reynolds number has a range of values from 1.09 x 10^6 to 3.47 x 10^6 [31].

Within this range of Reynolds values, fluidic behavior is known as chaotic and for this reason the equations that apply have a particular different effect from the classical theory of laminar flow where the Navier-Stokes equations have a prediction within a notorious level of accuracy [38].

An essential characteristic of turbulent flow is that is rotational, meaning that it has a certain level of vorticity. Vorticity $\omega(x,t)$ is the curl of the velocity

$$\omega = \nabla \times U \tag{2.56}$$

and is equal to twice the average of the fluid rotation at (x,t). The equation that defines the evolution of vorticity is obtained by calculating the curl of the Navier-Stokes equations [39]:

$$\frac{D\omega}{Dt} = \nu\nabla^2\omega + \omega \cdot \nabla U \tag{2.57}$$

The term related to pressure $\left(-\nabla \times \nabla\frac{p}{\rho}\right)$ vanishes due to incompressible flows or of constant density.

The equation that shows the evolution or rotation of an infinitesimal linear element of certain material $s(t)$ is the (2.58):

$$\frac{ds}{dt} = s \cdot \nabla U \tag{2.58}$$

On this equation, without considering the viscous term, it can be seen that is identical to the vorticity equation (2.56) [31]. Therefore, in the inviscid flow, the vorticity vector has the same behavior of an infinitesimal linear element of material, analysis that is known as the Helmholtz theorem.

If the average of the strain produced by the velocity gradients acts to contract the linear material element aligned with ω, then the magnitude of ω increases in the same manner. This phenomenon is known as *vortex stretching*, and is essential process in turbulent flows, and $\omega \cdot \nabla U$ is denoted as the term of vortex stretching [39]. The simulation of fluids in motion using Computational Fluid Dynamics, is based on the governing equations of fluid flow representing fundamentals of the laws of conservation of physics:

1. Conservation of the fluid mass.
2. The ratio of change of momentum is equal to the sum of the forces in a fluid particle. This statement comes from Newton´s Second Law.
3. The rate of change of energy is equal to the sum of the rate of the addition of heat and of the work done on a fluid particle. This statement comes from the first law of thermodynamics.

Conservation of Mass. The essential concept of mass conservation is to define mathematical equations to demonstrate that the rate of the mass increase in the fluid of the element is equal to the net change on the mass flow of fluid within the element [13]. Figure 2.7 shows the mass flow vectors entering and leaving the element volume.

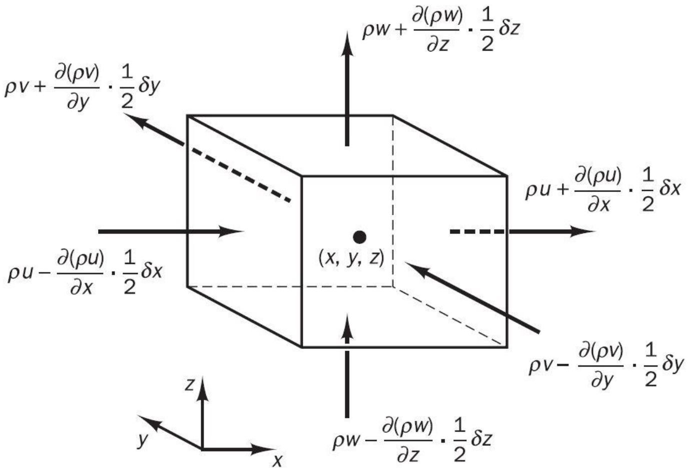

Figure 2.7: Mass flow vectors entering and leaving an element volume.

The rate of mass increase within the element is now equal to the net change in mass flow within the element across its faces. All the terms resulting from the mass balance are arranged in the left hand of the equation. It yields

$$\frac{\partial \rho}{\partial t} + \frac{\partial(\rho u)}{\partial x} + \frac{\partial(\rho v)}{\partial x} + \frac{\partial(\rho w)}{\partial x} = 0 \qquad (2.59)$$

using compact vector notation

$$\frac{\partial \rho}{\partial t} + div(\rho u) = 0 \qquad (2.60)$$

Considering that we are assuming incompressible fluid conditions, therefore the final equation of conservation of mass will be

$$\frac{\partial u}{\partial x} + \frac{\partial v}{\partial y} + \frac{\partial w}{\partial z} = 0 \qquad (2.61)$$

Conservation of Momentum. Newton's second law defines that the rate of change of the momentum of a fluid particle is equal to the sum of the forces on the particle. The rate of change of momentums per unit volume in a fluid particle at x, y, and z is given by [13]

$$\rho \frac{Du}{Dt} \tag{2.62}$$

$$\rho \frac{Dv}{Dt} \tag{2.63}$$

$$\rho \frac{Dw}{Dt} \tag{2.64}$$

Two types of forces on fluid particles can be distinguished: *surface forces* and *body forces*. Within the surface forces are those of pressure, viscosity and gravity, and within the body forces are the centrifugal, Coriolis and electromagnetic forces [40].

For practical purposes, contributions due to surface forces are considered as part of the general terms of the momentum equations and to include the effects of body forces, and source terms are used. Figure 2.8 shows the components of the surface forces as shear stresses.

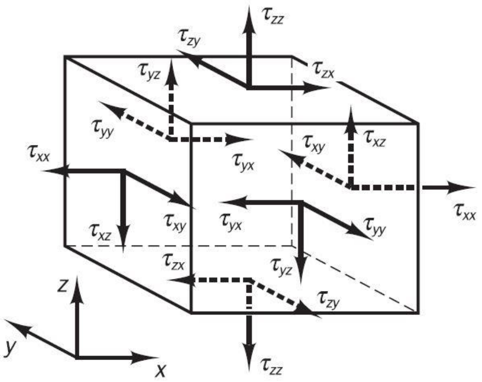

Figure 2.8: Components of the surface forces as shear stresses.

The *x, y* and *z* components of the momentum equation respectively are defined as follows

$$\rho\frac{Du}{Dt}=\frac{\partial(-p+\ \tau_{xx})}{\partial x}+\frac{\partial\tau_{yx}}{\partial y}+\frac{\partial\tau_{zx}}{\partial z}+\ S_{Mx} \tag{2.65}$$

$$\rho\frac{Dv}{Dt}=\frac{\partial\tau_{xy}}{\partial x}+\frac{\partial\left(-p+\ \tau_{yy}\right)}{\partial y}+\frac{\partial\tau_{zy}}{\partial z}+\ S_{My} \tag{2.66}$$

$$\rho\frac{Dw}{Dt}=\frac{\partial(-p+\ \tau_{xx})}{\partial x}+\frac{\partial\tau_{yx}}{\partial y}+\frac{\partial\tau_{zx}}{\partial z}+\ S_{Mx} \tag{2.67}$$

Conservation of Energy. The energy equation is derived from the first law of thermodynamics, which states that the rate of change of the energy of a fluid particle is equal to the ratio of the heat added to the particle plus the ratio of the work done on the particle [38].

$$\rho\frac{DE}{Dt} \tag{2.68}$$

Work. The ratio of work done on the fluid particle by a surface force is equal to the product of the force and the velocity component in the direction of the force. The ratio of the total work done on a fluid particle by a surface force is as follows:

$$\begin{aligned}&[-div(pu)]+\frac{\partial(u\tau_{xx})}{\partial x}+\frac{\partial\left(u\tau_{yx}\right)}{\partial y}+\frac{\partial(u\tau_{zx})}{\partial z}+\frac{\partial\left(v\tau_{xy}\right)}{\partial x}+\frac{\partial\left(v\tau_{yy}\right)}{\partial y}\\&+\frac{\partial\left(v\tau_{zy}\right)}{\partial z}+\frac{\partial(w\tau_{xz})}{\partial x}+\frac{\partial\left(w\tau_{yz}\right)}{\partial y}+\frac{\partial(w\tau_{zz})}{\partial z}\end{aligned} \tag{2.69}$$

Heat conduction. The net heat flux in a fluid particle in any of the three x, y, and z directions is given by the difference between the ratio of the input heat flux to the output heat flux on each respective Cartesian axis. The Figure 2.9 shows the heat flow in each of the geometric axes [15].

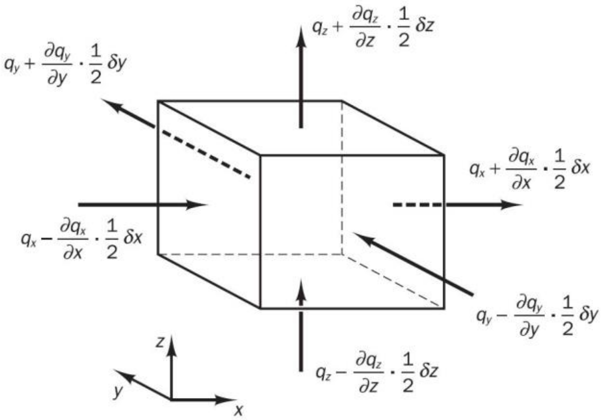

Figure 2.9: Mass flow vectors entering and leaving an element volume.

The following equations shows the Fourier's law of heat conduction taking as a reference the local temperature gradient.

$$q_x = -k\frac{\partial T}{\partial x} \tag{2.70}$$

$$q_y = -k\frac{\partial T}{\partial y} \tag{2.71}$$

$$q_z = -k\frac{\partial T}{\partial z} \tag{2.72}$$

These equations can be written in vector form as follows

$$q = -k \; grad\, T \tag{2.73}$$

General Energy Equation. Considering the general sum of body and surface forces, the general equation for energy balance is as follows [41]:

$$\frac{\partial(\rho h_0)}{\partial t} + div(\rho h_0 u) = div(k\ grad\ T) + \frac{\partial p}{\partial t} + [\frac{\partial(u\tau_{xx})}{\partial x} + \frac{\partial(u\tau_{yx})}{\partial y} + \frac{\partial(u\tau_{zx})}{\partial z} + \frac{\partial(v\tau_{xy})}{\partial x} + \frac{\partial(v\tau_{yy})}{\partial x} + \frac{\partial(v\tau_{zy})}{\partial x} + \frac{\partial(w\tau_{xz})}{\partial x} + \frac{\partial(w\tau_{yz})}{\partial y} + \frac{\partial(w\tau_{zz})}{\partial z}] + S_h \tag{2.74}$$

General Equilibrium Equation. All the effects caused by viscous stress in the internal energy equation are described by the dissipation function, which can be described using the Newtonian model for the viscous effects in the equation of internal energy. It can be described as follows [41]:

$$\rho \frac{Di}{Dt} = -p\ div\,\boldsymbol{u} + div\ (k\ grad\ T) + \Phi + S_i \tag{2.75}$$

Deep Learning Theory.

Much of the current communication technology is based on machine-learning analysis. From systems used to identify objects in images, store historic searches to make later recommendations to users, filtering social networks, as well as scientific applications to predict physical phenomena [42].

Deep Learning can be defined as a neural network with more than two layers. A neural network is a set of algorithms that is named this way, because it behaves like how human neurons learn, meaning, through repetitive approaches relating certain experiences to certain results. They are designed to recognize patterns [43]. As neurons do, these algorithms learn from data to relate initial conditions to final responses identifying the pattern. At the end, the network delivers the outputs based on the inputs and the pattern that previously trained the network.

The most common deep learning analysis is the one known as supervised learning, which in every set of data that is fed into the system, compares the results to verify how accurate the model is predicting the outputs and then it goes into the next layer [44]. Figure 2.10 demonstrates the model:

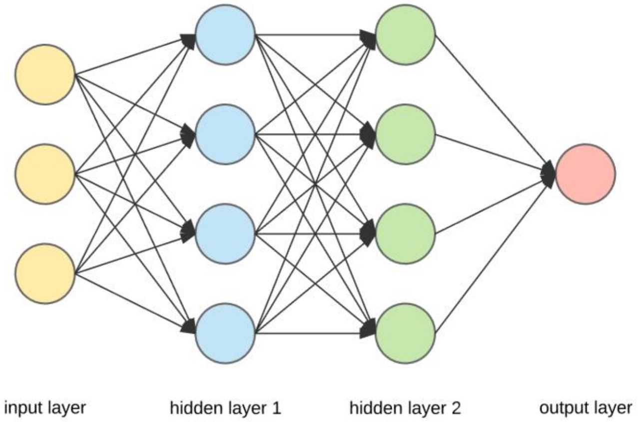

Figure 2.10: Graphic definition of the neural network algorithm.

As can be seen in Figure 2.10, the neural network is made up of a variety of nodes that are connected and communicated with each other. Each node takes multiple inputs and makes dot products with each weight as observed in the equation (2.76). Then it applies an activation function to the product of the inputs and generates an output [45].

$$[x_1 \quad x_2 \quad x_3] \cdot \begin{bmatrix} w_1 \\ w_2 \\ w_3 \end{bmatrix} + [b] = x_1 w_1 + x_2 w_2 + x_3 w_3 + b \tag{2.76}$$

This product is then used as input for the activation function. The activation function acts as a switch and depending on the function, the value can be between 0 and 1 or -1 and 1. It is a common practice that for the activation function, any of the following is used: Sigmoid or ReLu (Rectified Linear Unit) [44].

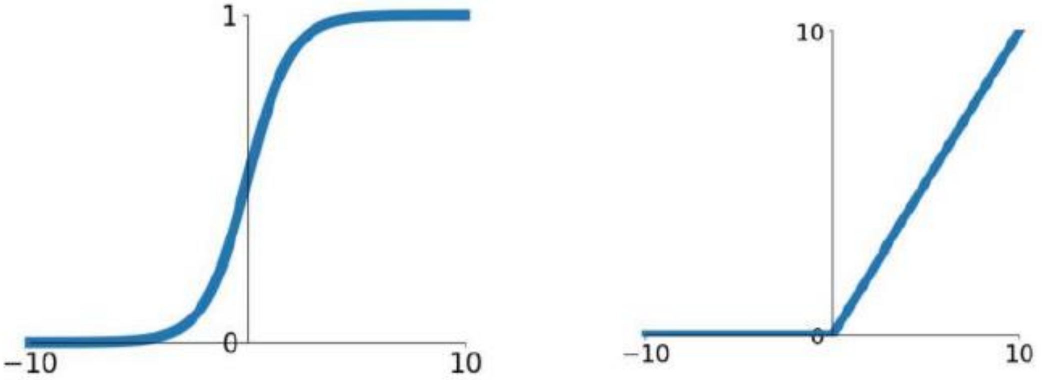

Figure 2.11: Sigmoid Function (Left), ReLu Function (Right)

Once the activation function is calculated, the output denoted by h is then determined.

$$h_1 = f(x_1 w_1 + x_2 w_2 + x_3 w_3 + b) \tag{2.77}$$

The activation function is denoted by *f.* In neural networks there are two components: the linear component that is the linear algebra and the non-linear component that is the activation function [43].

The hidden layers are giving weights to the different inputs according to the previous training of neural network. Based on this weighing, the algorithm is filtering the data to get the best result possible.

$$h = f\left(\begin{bmatrix} w_{11} & w_{12} & w_{13} \\ w_{21} & w_{22} & w_{23} \\ w_{31} & w_{32} & w_{33} \end{bmatrix}\begin{bmatrix} x_1 \\ x_2 \\ x_3 \end{bmatrix} + \begin{bmatrix} b_1 \\ b_2 \\ b_3 \end{bmatrix}\right) \tag{2.78}$$

A certain number of hidden layers help to reduce the size of the error; nevertheless, it is important to identify and an optimum number of hidden layers and the number of internal units because it is possible to increase the error if we continue increasing the number if hidden layers infinitely.

Since the beginning of the pattern recognition, the goal of the researchers has been to replace features designed by the engineer's hand with multilayered networks, but despite its simplicity, this concept was not understood until the mid-1980s. Multilayered architectures can be trained by a simple descending stochastic gradient [46].

The backpropagation procedure to calculate the gradient of an objective function with respect to the weights of a group of multilayered modules is nothing more than a practical application of the chain rule used to calculate derivatives. The key point is that the derivative or gradient of the objective function with respect to the input of a module can be calculated by working back from the gradient with respect to the output of the module (or the input of the subsequent module) [47].

The process of the equation (2.78) is a matrix multiplication followed by an activation function; this will solve the hidden layer and the process will be repeated to determine the adequate weights for the problem. At the beginning of constructing the neural network, the weights are initialized through a Gaussian random number generator. At the start of the construction of a neural network, the weights are initialized using a Gaussian random generator. The goal is to adjust the neural network weights to get better predictions every time. This is accomplished by varying the weights to minimize the error between the input and the predicted data. To achieve this, it is needed to implement a backpropagation descending gradient.

$$w = w_o - \alpha * \Delta\, error \tag{2.79}$$

The descending gradient method is based on the gradient that makes a change to the new weight value w. It takes the current position w_o and adjust it with the error weighted by a step size α. The crucial component in a neural network is the loss function. Optimizing the algorithm is based on minimizing this loss function. This type of algorithm is called of *supervised training*, so the algorithm is intended to learn from a series of data to make predictions.

For a given training pair, the input data will be called x^z and the desired output or prediction will be y^z. Thus, J is the loos for the training of that pair x^z.

$$J(w, b, x, y) = \frac{1}{2}\left\|y^z - y_{pred}(x^z)\right\|^2 \tag{2.80}$$

The variable $y_{pred}\ (x^z)$ is the output layer of the neural network in. To generalize the cost function and include more than one training pair, it is necessary to minimize the function for all m training pars:

$$J(w, b) = \frac{1}{m}\sum_{z=0}^{m}\frac{1}{2}\left\|y^z - y_{pred}(x^z)\right\|^2 \tag{2.81}$$

To determine the new weights the descending gradient and bias for each weight will be calculated through the equations (2.82) and (2.83):

$$w_{ij}{}^{(l)*} = w_{ij}{}^{(l)} - \alpha\frac{\partial}{\partial w_{ij}{}^{(l)}}J(w, b) \tag{2.82}$$

$$b_i{}^{(l)*} = b_i{}^{(l)} - \alpha\frac{\partial}{\partial b_i{}^{(l)}}J(w, b) \tag{2.83}$$

The way neural networks work is through an initialization of the weights. Then, the information is feedforward to calculate the predicted value. At the end, the predicted value and the fed value can be taken to determine the loss function. Through the backpropagation and the descending gradient, weights and bias can be adjusted [48].

From the above calculations, the importance of the activation function can be appreciated. Whenever the output of the activation function is close to zero, there will be no information to adjust the weights when using the descending gradient. This is how neural networks learn and adjust to exclude unnecessary values. When the weights are not adjusted, we realize that our numerical network has converged.

In the case at hand, this type of multilayered architecture was used to predict parameters located in cartesian coordinates x, y and z but with no equidistant spaces, so an equidistant model was designed and the neural network algorithm was trained to predict what would be the values of that same geometrical model would but on an equidistant set of cartesian coordinates [46].

The Background and Literature review section has presented in detail the theoretical foundations that were used for the present study. It is noteworthy that in the Deep Learning section the specific case of a neural algorithm that is called supervised was presented. However, within this same category, there are additional routines or algorithms particularly used for image detection, such as the Convolutional Neural Network, which were not used in the present study, but represent a huge component of Neural Networks.

Chapter 3. Problem Definition.

The section of the Problem Statement presents the details of the case of the study for this dissertation and the way the theoretical tools from the Background and Literature Review would be used to face the problem. The fundamental component of the Problem Definition is explaining the general conditions, tools, and impediments to perform the study, particularly the scaled analysis that, as explained during the chapter, was one of the greatest challenges. The purpose of scaling the original geometry in a virtual model has been to perform simulations that would allow me to generate the temperature profiles that will finally take me to the calculations of C_T^2 and C_n^2.

After this introductory paragraph, I return to the concepts presented in the Introduction chapter to state the purpose of this study. The main objective of the present dissertation is to find a mathematical relation between the atmospheric Reynolds number under turbulent conditions and the structural constant of refractivity C_n^2. The reason is that the presence of strong turbulence in the atmosphere along a laser propagation path affects the quality of the laser-based communication systems. Thus, to improve the quality of image detection and target selection in the presence of turbulence there is a need for characterizing these conditions [49].

This characterization is achieved by finding the mathematical trend between the turbulence conditions in the atmosphere and the variations of the optical parameters. The parameters that were chosen to find this mathematical relation were the Reynolds number and the structural constant of refractivity C_n^2.

There is a location at Maui, Hawaii, where Air Force Research Laboratories (AFRL) communicate at the top of two mountains named Mauna Loa and Haleakala using optical devices. These laboratories are particularly interested in developing these new metrics for deep turbulence effects on laser propagation through a long path. To be able to make the necessary adjustments to their devices depending on the instantaneous turbulent conditions and thereby improving the performance of their optical communication.

An important point to face this problem has been the calculation of C_n^2 that requires the calculation of C_T^2. The structural function of temperature requires the temperature profile of the geometry under analysis. Because experimental information on temperatures was not available, it was decided to generate this information through a CFD simulation. The biggest challenge I was faced with was scaling the model to a level that could be studied by computational means but could replicate the original conditions to simulate as closely as possible [50].

To create the model, it was necessary to limit the original geometry. Because the height of both mountains is around 3 km, we decided to double the height to 6 km to cover a complete volume. The dimensions were 6 km height, 2 km width and 150 km of length. The distance of 2 km depth was used to cover a sufficiently wide area where atmospheric temperature variations, as a result of turbulence, can have consequences in refractive conditions affecting the laser´s path in consequence [41].

Figure 3.1 shows the dimensions of the original geometry and a representation of the typical turbulent atmospheric conditions between the two mountains. Note the doubling of the height mentioned previously to cover an area of turbulence greater than just the height of the mountains.

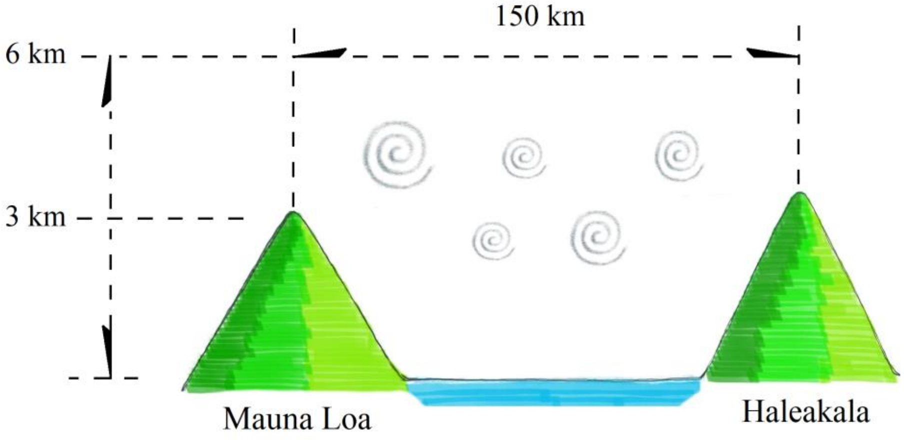

Figure 3.1: Original geometry dimensions.

The initial 3D model was created in a software named NX. Due to the large geometry of the real model where the length is 150 km, to fit the geometry into a 3D computational model, it was decided to perform a scaling down of 10,000: 1. Figure 3.2 shows the dimensions for the scaling down step.

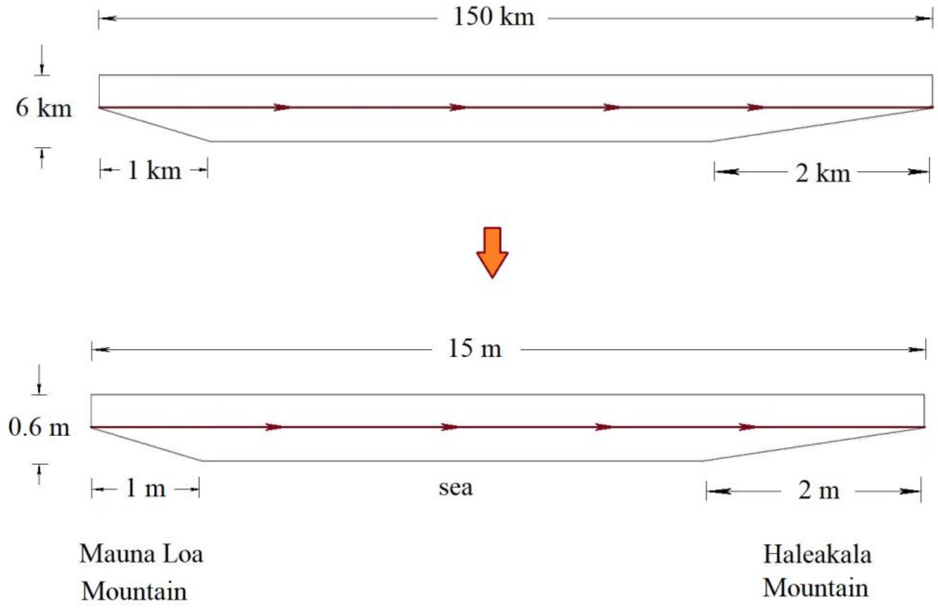

Figure 3.2: Scaling down the geometry.

Figure 3.3 shows the final dimensions of the model. The length was trimmed so the lateral dimensions were clearly observed.

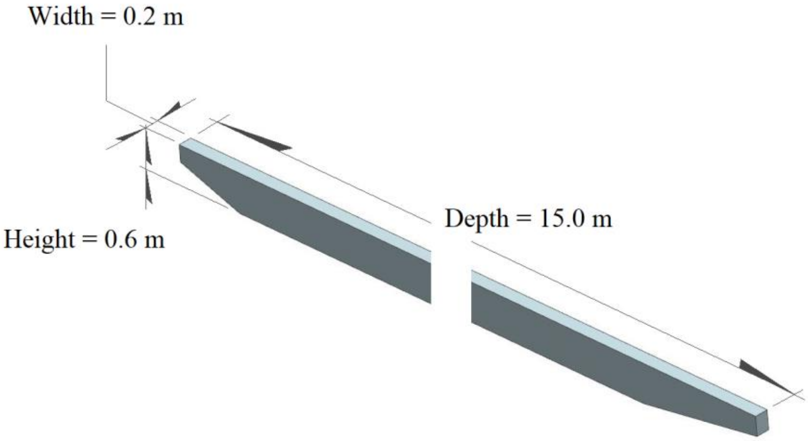

Figure 3.3: Final geometry dimensions.

Justification. For the model to be analyzed using the CFD ANSYS Fluent simulation software, a scaling of 10,000: 1 was necessary.

The scaling dimensional factor was calculated based on the original length and the proposed length of the model [51]:

$$\frac{L_o}{L_s} = \frac{150{,}000\,m}{15\,m} = 10{,}000 \tag{3.1}$$

Where L_o is the original length and L_s is the length in the scaled model. Both or the dimensions are in meters.

Velocity conditions. Following these scaling conditions, the next step was to define the values of the properties to be used in the scaled model, so I started with the velocity.

Based on the range of 5 to 16 m/s of the original model I performed the scaling down of the velocity of 5 m/s.

$$v_s = \frac{v_o}{10{,}000} = 5 \times 10^{-4}\ m/s = 0.5\ mm/s \tag{3.2}$$

However, because the appropriate conditions for turbulence are the same in the original and in the scaled model regardless of the dimensions, scaling down velocities 10,000 times does not produce the turbulence conditions required for my analysis. Not even scaling down the velocities 10 times. If the turbulent conditions cannot be reproduced, the effects over the diffraction index cannot be calculated [51].

For this reason, I decided to maintain the same velocities that generate the same turbulent conditions of the original geometry even though the volume of fluid as well as the inlet area have decreased 10,000 times.

Temperature conditions. The basis for performing the analysis of the changes in the constant of diffraction index C_n^2 are the temperature gradients. In a 10,000:1 scaled model there is virtually no temperature change between the bottom and the top of the model, not even one-degree Celsius.

The temperature in the original model varies from 25 °C at sea level to 5.5 °C degrees at the lasers path. For this reason, it was decided to repeat this linear temperature gradient in the scaled model to simulate the temperature variations affected by the turbulence conditions. An important point to consider is that the temperature at sea level is estimated at 10 °C less than the surface of the ground at similar height, however, the ambient temperature scale that was used started from 25 °C since the temperature over the sea, takes a high gradient few meters above it, equaling the temperature scale of the atmosphere that initiates at ground level.

Pressure conditions. Because pressure conditions require to be linked to temperature to maintain adequate density conditions, it was also decided to set the original manometric pressures over all the model.

Testing. I performed numerous tests, more than 1000 CFD Simulations, to verify that the boundary conditions explained on this scaling justification are the closest possible to simulate the original model conditions.

Figures 3.4 and 3.5 show the comparative simulation of the velocity in the case of scaling down the temperature and pressure conditions vs maintaining the original ones. The low precision presented by the case of the scaled conditions can be clearly observed with respect to the original ones [52]. It can be seen in Figure 3.4 that there are no turbulence conditions and that the velocity gradient becomes uniform, decreasing to minimum motion points after half the volume of flow.

On the other hand, Figure 3.5 shows a fully developed turbulent behavior where the temperature variations can be clearly observed. The simulation shows zones of high level of turbulence throughout the flow volume and in the second half, high zones of velocity variations are perceived. These zones have rotational systems dissipating an important part of the energy in the form of heat.

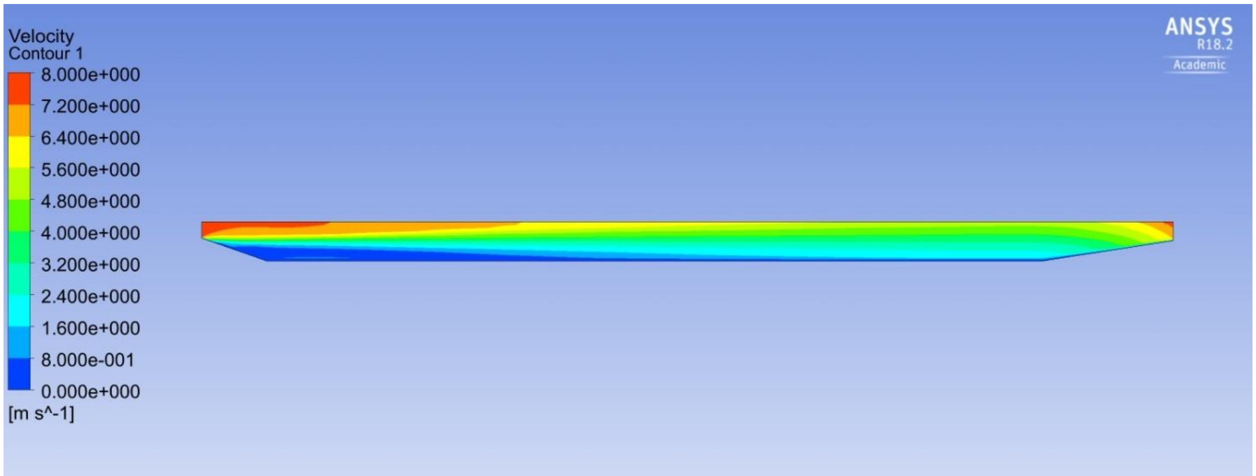

Figure 3.4. Velocity simulated with scaled conditions.

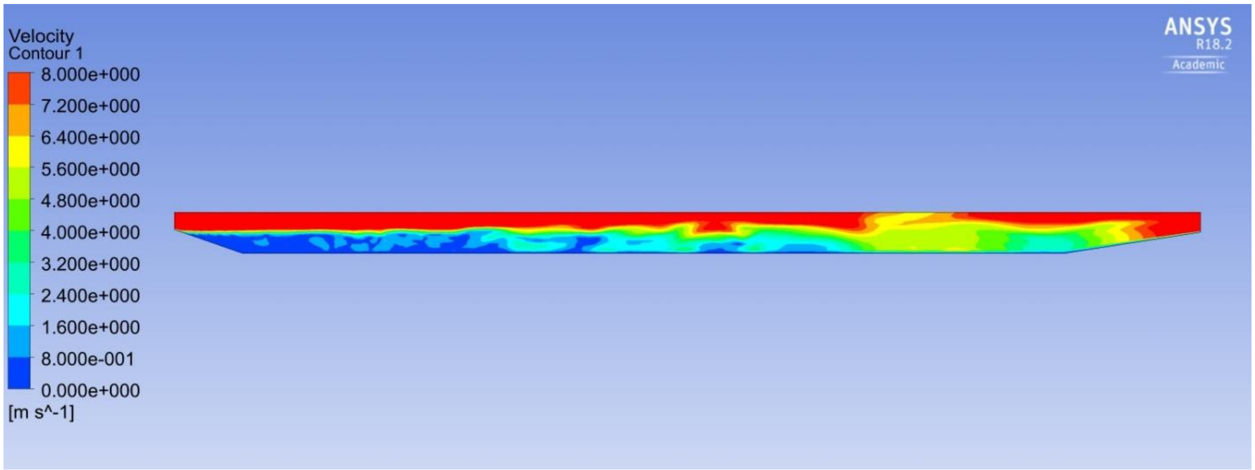

Figure 3.5. Velocity simulated with original conditions.

Additionally, Figures 3.6 and 3.7 show the behavior of the temperature with scaled conditions vs original one. There is practically no profile of temperature variations in the case of the scaled model, but the profile for the case of temperatures in the original model is very clear.

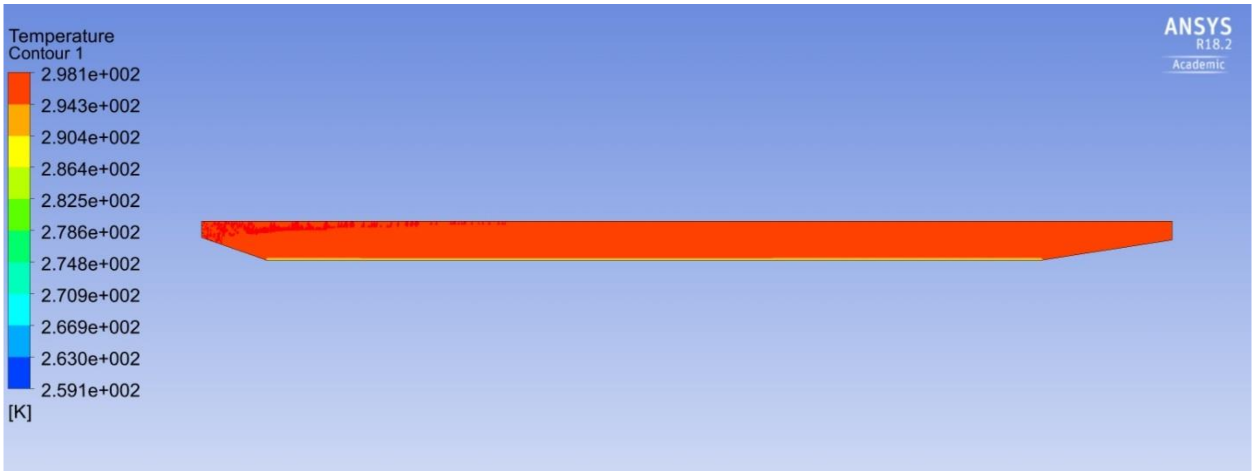

Figure 3.6. Temperature variations simulated with scaled conditions.

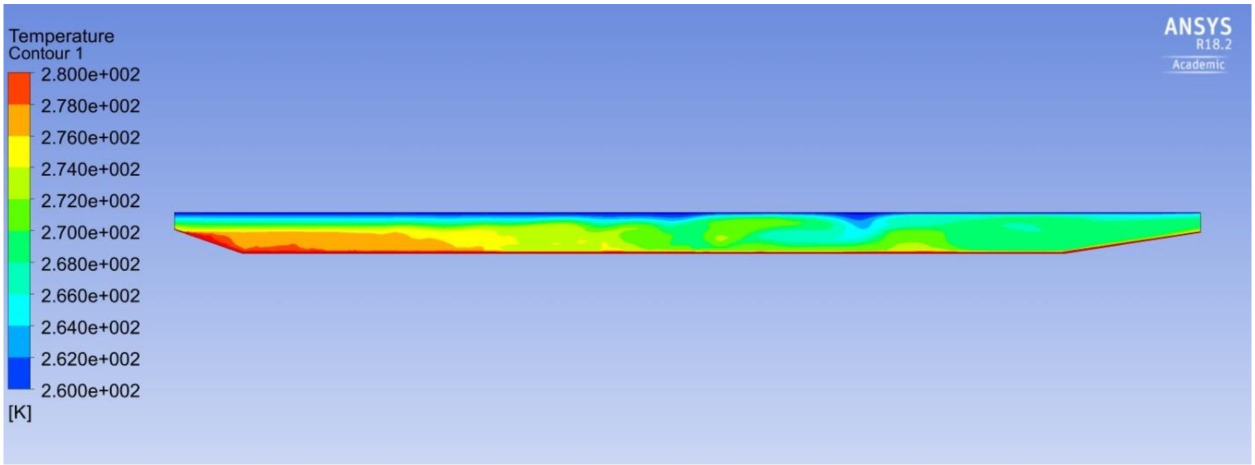

Figure 3.7. Temperature conditions simulated with original conditions.

These series of 1000 simulations allowed me to define that effectively, in the case at hand, the use of the velocity, temperature and pressure conditions of the original geometry, it is the best option to simulate the turbulence conditions necessary to necessary to obtain the adequate information for my study [53].

This allows me to conclude that the simulation that was carried out during the present work has an acceptable degree of precision.

Modeling. The CFD simulation software that was used to obtain the temperature, pressure and velocity profile was the ANSYS Fluent [54]. This tool has several sections that are shown in the Figure 3.8 and will be explained below.

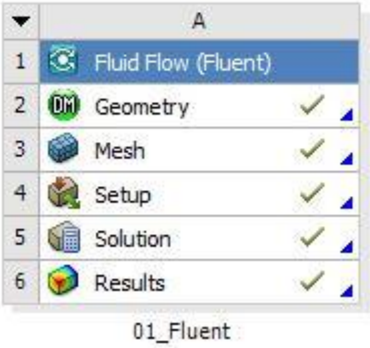

Figure 3.8: ANSYS Fluent Sections for fluid analysis.

In the *Geometry* section the tool can generate the geometric profile that needs to be analyzed or imported in general *.iges* format from any other design software. In my case I used NX to generate the geometry and import it to ANSYS through its module called *DesignModeler*. The Figure 3.9 shows the geometric profile of the case.

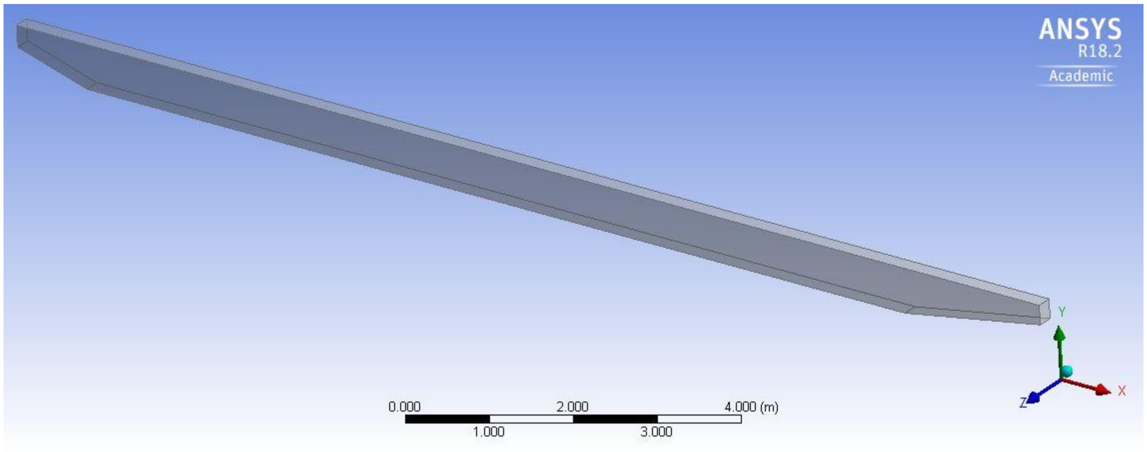

Figure 3.9: 3D ANSYS solid model of the case under analysis.

Meshing. The section named *Mesh* is where each part of the model is defined; after this, the sensitive mesh can be generated. The mesh allows the generation of the general simulation. In Figure 3.10 the named sections can be seen inside the design tree. In Figure 3.11 the named sections are shown on the solid model [54].

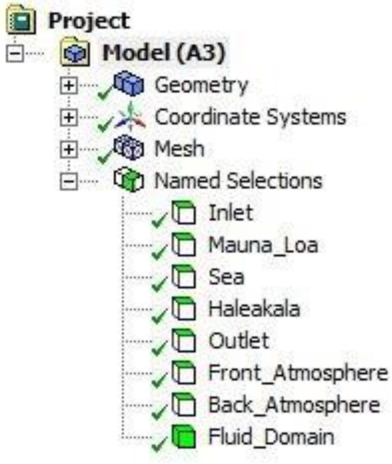

- Project
  - Model (A3)
    - Geometry
    - Coordinate Systems
    - Mesh
    - Named Selections
      - Inlet
      - Mauna_Loa
      - Sea
      - Haleakala
      - Outlet
      - Front_Atmosphere
      - Back_Atmosphere
      - Fluid_Domain

Figure 3.10: Design tree for the ANSYS Meshing section.

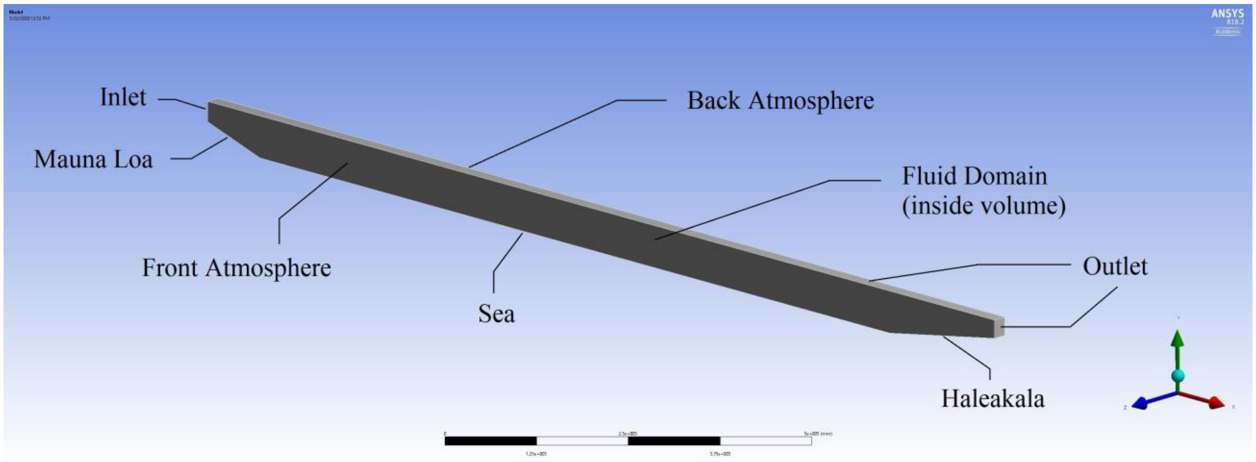

Figure 3.11: Designation of named sections according to the original model.

After the corresponding sections have been named, the mesh size is established through the command called *edge sizing*. In this case an edge size of 20 mm was defined. The figure shows the edges of the model selected with a division of 20 mm.

The reason I selected a 20 mm for the elements dimension is because it was the smallest possible dimension to reach the maximum limit of 500,000 element in the ANSYS Fluent because I used a student license. This selection on Figure 3.12 precedes to the generation of the mesh.

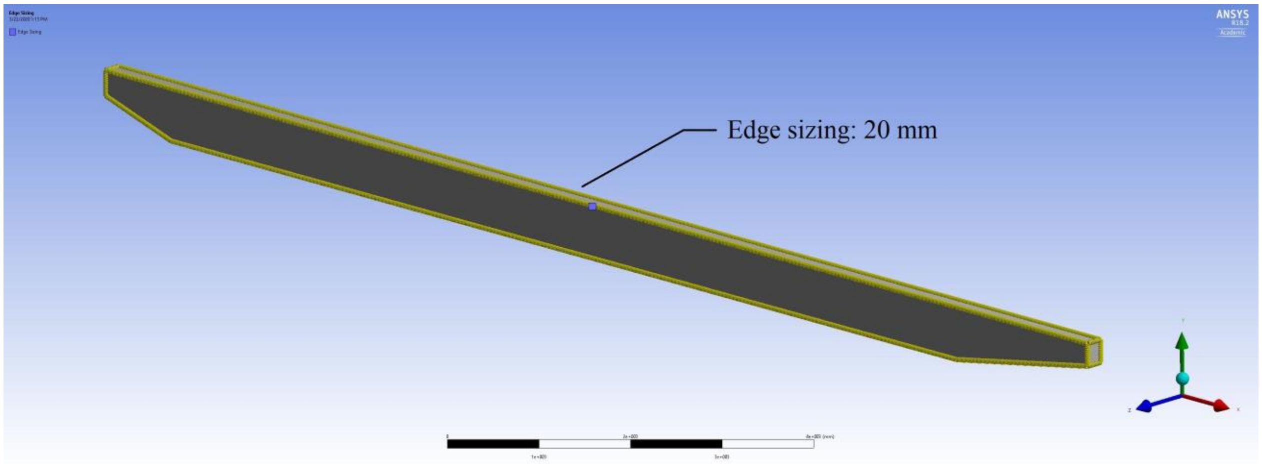

Edge sizing: 20 mm

Figure 3.12: Edge dimensioning for defining the element size of the mesh.

In Figure 3.12 the final mesh can be seen. It has 450,000 tetrahedral elements and 550,000 nodes. This mesh represents components of a matrix that will receive the values of the fluid properties using the fundamental fluid equations.

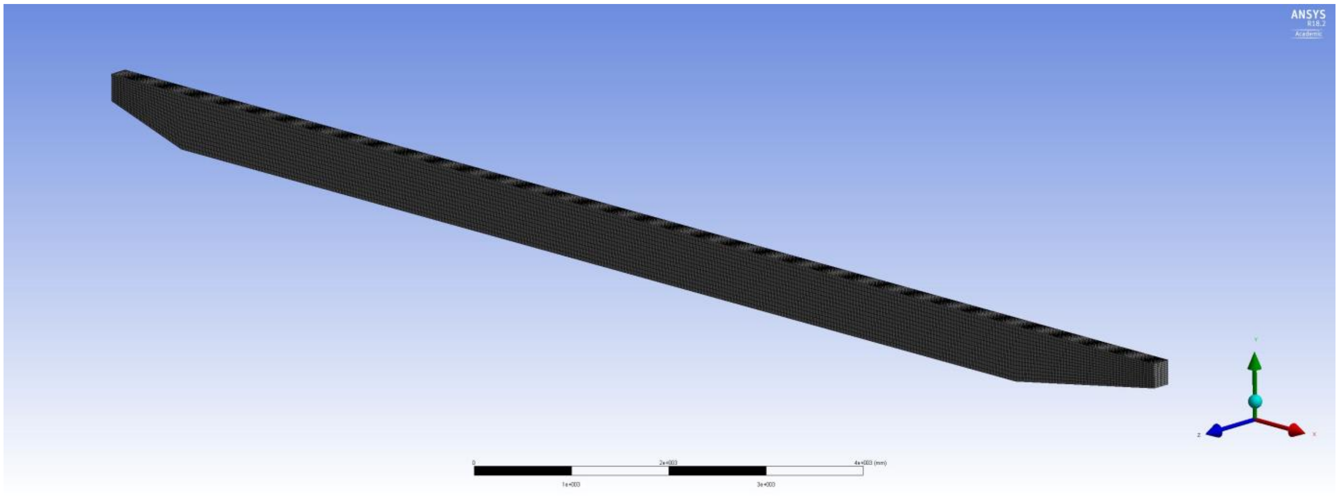

Figure 3.13: 3D mesh with 20 mm side elements.

Defining Boundary Conditions and Setting Up the Model. In the *Set up* section all the boundary conditions are defined. These data are fed on the three divisions shown in Figure 3.14.

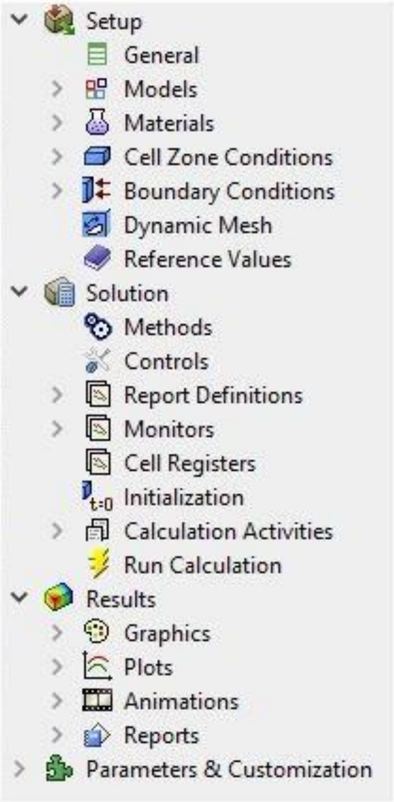

Figure 3.14: Components of the *Set up* section in ANSYS Fluent.

In the *Models* section of the *General* modules, the type of analysis that will be performed is defined. In my case, since it involves heat flow, it is necessary to indicate that it will be using in the Energy´s mathematical modules [37]. On the other hand, the mathematical model that I considered most suitable for its precision when simulating turbulent conditions is the LES (Large Eddie Simulations). I selected this option inside the *Viscous Model* section.

In the *Materials* section I specify *air* as the working fluid. In the *Cell Zone Conditions* the pressure and temperature conditions were specified according to the range of values that are defined in the *Chapter 4. Methodology* of this dissertation.

Finally, the model is initialized and run with all the data supplied [38]. At the end, a data profile with the velocity, temperature and pressure by coordinate can be generated in a .csv file in the *Solution* section.

Neural Network Analysis. Mathematical Background. In the present study, the first part has consisted in generating data of the profile of atmospheric temperatures, pressures, and velocities. Subsequently, to calculate the structural constant of the refractive index, the following equation is required [6]:

$$D_T = \langle [T_r(r_1 + r) - T_r(r_1)]^2 \rangle \tag{3.3}$$

After the structural function of the temperature has been calculated, the equation 3.5 is used to obtain ${C_T}^2$. This equation was previously defined in Chapter 3:

$$D_T = {C_T}^2 r^{2/3} \tag{3.4}$$

Then, clearing ${C_T}^2$ from the equation I have

$$C_T{}^2 = D_T/r^{2/3} \tag{3.5}$$

Finally, with the set of values obtained from the structural constant of the temperature $C_T{}^2$ in addition to the values of Pressure and Temperature at the height of the laser´s path, I use the equation 3.9 to obtain $C_n{}^2$ [11]:

$$C_n{}^2 = \left(\frac{79\,P}{T^2} \times 10^{-6}\right)^2 C_T{}^2 \tag{3.6}$$

Thus, through this process I obtain the value of the structural diffraction constant $C_n{}^2$.

On the other hand, the reason I relied on the use of neural networks was to predict the temperature on equidistant coordinates to be able to calculate the structural function of temperature. It can be observed from the equation (3.6), that the quadratic difference requires a constant value of positional vector *r*. For the equation to have accuracy, the data has to be placed on an equidistant mesh.

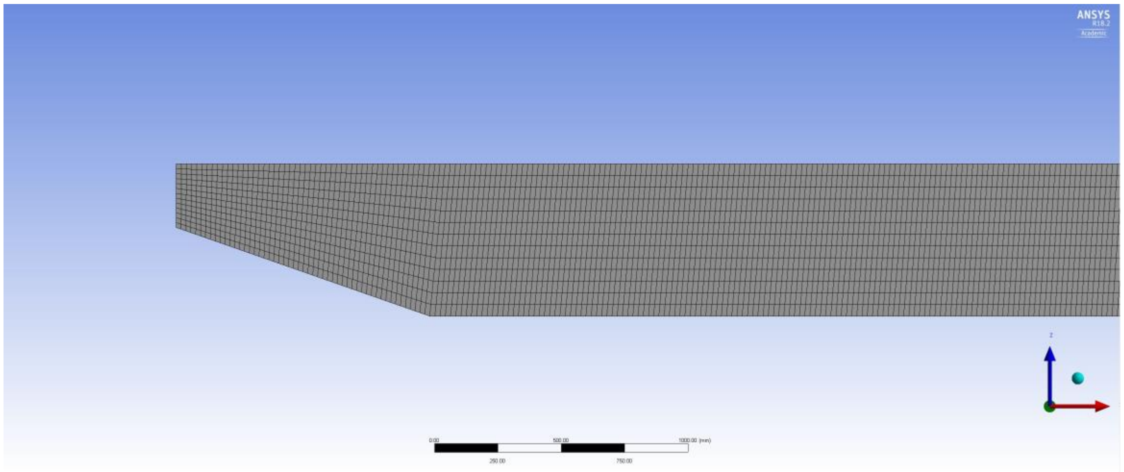

Figure 3.15: Close view of the non-equidistant mesh generated in ANSYS Fluent.

The Figure 3.17 shows the detail of the mesh. It is possible to observe notorious variations in the element sizes which side specification is 20 mm.

Neural Network Process. Importing Data. The procedure to transform the non-equidistant mesh to an equidistant set of coordinate values is using a neural network algorithm. Thus, that step after running the cases from the ANSYS Fluent, was to export the data of velocity, temperature, pressure of the entire volume in .csv format. This data was then imported into a script in Python language [55].

Inside the Python code, that was created in a Spyder platform, the imported .csv file was used to create a matrix of data. Parallel in the script, an equidistant array of coordinates with side 20 mm was created. Figure 3.16 shows the matrix.

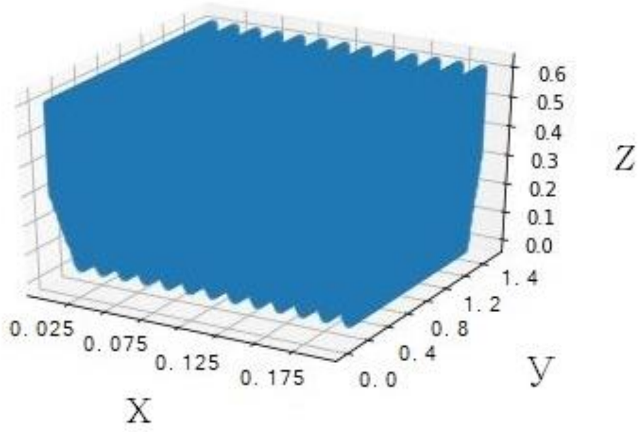

Figure 3.16: Equidistant points created to simulate the original model.

In the figure 3.16, each coordinate is represented by a blue sphere, the union of all these spheres is the diagram presented.

Training the Algorithm. The next step is training the neural network algorithm. The algorithm used was the *MLPRegresor* that belongs to the *sklearn.neural_network* library. *MLPRegresor* means *Multi-Layer Perpectron Regresor* and is a model that optimizes the squared-loss using stochastic gradient descent [43].

Selecting the Data. The process for prediction begins with the selection of data from the .csv file imported from ANSYS Fluent to create two groups of variables (*X*, *Y*) selected for training. One of them, the *X*, containing the set of coordinates and the other one corresponding to the temperature. This process is shown in equations (3.7) and (3.8).

$$X = df.loc[:,['x-coordinate','y-coordinate','z-coordinate']] \tag{3.7}$$

$$Y = df.loc[:,['temperature']] \tag{3.8}$$

Training. Later comes the training section. Based on the set of values *X* and relating it to *Y* results, the training comes with a set of values over the 80% of the training data and testing this prediction with 20% of the data from the same set of values. Equation (3.9) shows this process.

$$X\_train, X\_test, Y\_train, Y\_test = train\_test\_split(X, Y, random\_state = 42, test\_size = 0.20) \tag{3.9}$$

Prediction Process. The next step is to use the neural network algorithm to make the prediction. This algorithm is the *MLPRegressor* and its commands can be seen in equations (3.10) and (3.10). The algorithm uses the solver ***adam*** and the activation function is ***relu***. In the commands shown, ***6*** hidden layers were used as well as ***13*** neurons inside each hidden layer,

$$Y\_clf \ = \ MLPRegressor(hidden\_layer\_sizes = (13, 13, 13, 13, 13, 13), \\ solver = 'adam', activation = 'relu') \tag{3.10}$$

$$Y\_predict \ = \ Y\_clf.predict(X\_test) \tag{3.11}$$

Optimization. The number of hidden layers as well as the number of neurons per hidden layer mentioned, were carefully chosen through an optimization process. This process was carried out through calculating the value of the error in the prediction.

The error in the prediction was calculated by the difference between the predicted and the initial values previously fed into the algorithm. This process was done using different cases of number of hidden layers vs number of neurons by varying both concepts from 2 to 20, respectively [56]. This difference is shown in equation (3.12).

$$err\_sum \ = \ Y\_predict \ - \ Y\_test\_flat \tag{3.12}$$

To avoid negative numbers, the error was squared as shown in the equation (3.13)

$$err\_sum \ = \ err\_sum ** 2 \tag{3.13}$$

The minimum value of error was found to be ***6*** hidden layers with a size of ***13*** elements each layer.

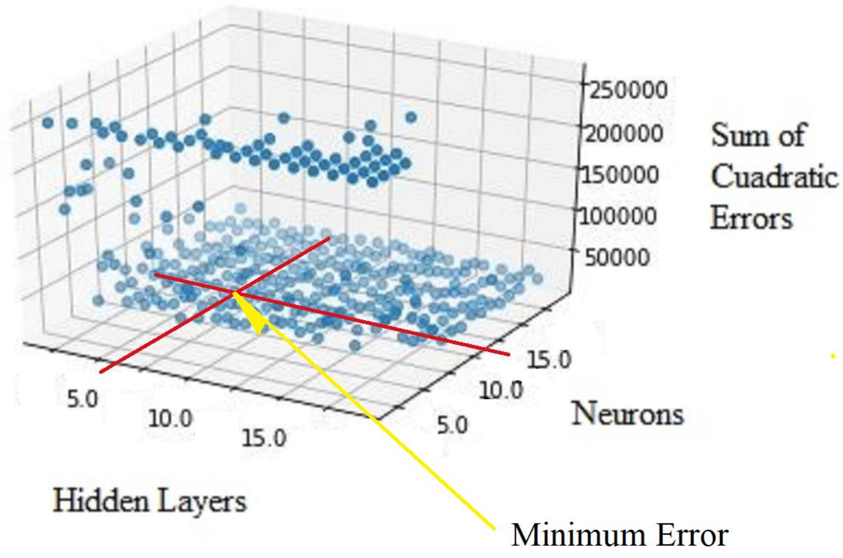

Figure 3.17: Distribution of the errors Hidden Layers vs Neurons.

The Figure 3.17 shows the distribution of the errors when the number of hidden layers is varied with respect to the number of elements per layer. It can be seen that errors are very high when the number of hidden layers is varied but the number of elements per layer is kept low like from 2 to 5 elements, especially if the number of layers is high and the number of elements is low [48].

Mesh comparison. Although the resultant mesh will be presented with all the results in Chapter 10, Figure 8.6 shows the objective pursued with the use of the neural algorithm.

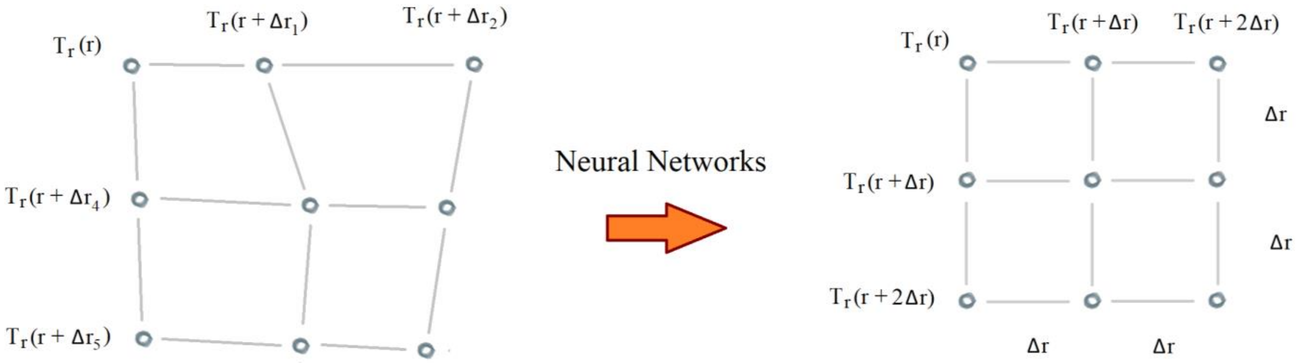

Figure 3.18: Mesh comparison of meshes before and after Neural Network algorithm.

This Chapter about Problem Definition allowed me to present all the challenges I faced in order to find a relation between the Reynolds number and the structural diffraction constant C_n^2, particularly when scaling the model and choosing the adequate properties of temperature and pressure, as well as the adequate velocities to reproduce the original conditions.. It is important to mention that the support of Dr. Kumar and his research team, like Arturo Rodriguez, was extremely important for finding the right geometry and properties to simulate the original conditions. On the other hand, Dr. Munoz's support in neural networks as well as the use of his High-Performance Computers (HPCs) was crucial for the generation of a defined temperature profile in an equidistant coordinate network to finally calculate the values of C_T^2 and C_n^2 [46].

Chapter 4: Methodology.

The research problem or question to investigate is finding new metrics for deep turbulence effects on laser propagation through a long path. Since the most representative parameter of the level of turbulence is the Reynolds number, and, on the other hand, a representative optical variable is the constant of refractive index C_n^2, the research has been focused on finding the mathematical relation between both variables [57].

To perform the Reynolds number calculations, it was necessary to identify the range of velocities present at the location, as well as the kinematic viscosity and the representative length. The typical range of velocities was found to be from 5 to 16 m/s. The characteristic dimension L is 3 m, which is the laser´s aperture and the kinematic viscosity ν is equal to 1.506×10^{-6} m^2/s.

On the other hand, the calculation of the structural constant of the diffraction index C_n^2 is directly related to the structure constant of the temperature C_T^2, which requires a set of temperature data in equidistant coordinates for the entire geometric volume under analysis to use the equation previously defined in Chapter 3 [53].

Most of my research work was focused on the collection of temperature data for the calculation of C_n^2, and since I did not have access to experimental information on the temperatures read at the geographical location under study, I had to generate it by other means.

The generation of these data was represented by two stages: the first, by the entire sequence of temperature profiles related to series of CFD simulations based on each case of velocity. I established this sequence of velocities within the range of 5 to 16 m/s with a step size of 0.25 m/s, generating a total of 45 cases [57].

From each case of velocity that was simulated in the CFD, a profile of temperatures was generated and exported into a .csv file in order to calculate C_T^2 and, in turn, the corresponding calculation of C_n^2. The generated profiles are defined in non-equidistant coordinates, but they need to be on equidistant ones for using the structural temperature equation.

It is important to note that when I made a series of adjustments to the volume in the meshing step during the C*FD* simulation, the spatial coordinates were very close to being equidistant. However, it was not achieved exactly [22]. Because of this, I decided to do an additional step that would allow me to achieve this equidistant mesh.

This additional step focused on the use of neural networks. As reviewed in Chapter 3, Neural networks are computational algorithms that can predict values, based on a series of data with which they are trained. The data used to train this algorithm were the temperature profile along with the corresponding coordinates. After training, the algorithm was asked to predict the temperatures that corresponded to an equidistant mesh that was provided. The generated temperature profile was the one that was being searched [34].

The next step was to relate the values of the Reynolds number with respect to the values found for the structure refractive index constant C_n^2 in a table. These are the results presented in the conclusions section for discussion.

The first part of the methodology consisted of identifying the general atmospheric conditions for calculating the Reynolds numbers from equation (4.1). An important component is the range velocities previously identified from 5 to 16 m/s. Other components are the characteristic dimension L, which is the laser´s aperture and has a value of 3 m, and the kinematic viscosity ν, which is equal to 1.506 x 10^{-6} m^2/s.

$$Re = v\, L/\nu \tag{4.1}$$

The calculations result in a range of Reynolds values from 1.09 x 10^6 to 3.47 x 10^6. Since the value for the transition between laminar to turbulent is 5 x 10^6, the entire range of Reynolds numbers is under turbulent conditions.

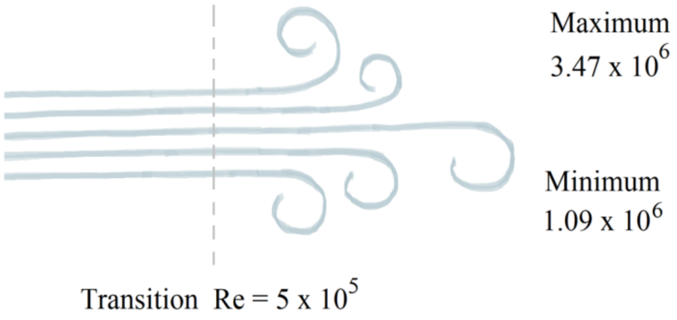

Figure 4.1. Range of Reynolds numbers.

The second part consisted of data collection for the calculation of C_n^2. As previously mentioned, the calculation of the structure constant of the refractive index C_n^2 depends on the value of the temperature structure constant C_T^2 that in turn depends on the temperature profile [58]. However, since I did not have access to this experimental information, I used a computational simulator to generate it.

To perform this simulation, it was important to first delimit the geometry that would be replicated and scaled for in a computational parametric model. This process of scaling the original geometry as well as its justification has been explained in detail in Chapter 3. In this chapter I explain in detail the use of specific data to generate the simulation cases, as well as the methodology to generate the temperature data for the calculations of C_T^2 and $C_n^{2.}$

In the conditions of the original model, the laser beacon platform is located at the summit of the Mauna Loa at an elevation of 3,058 m and the receiver telescope at the summit of Haleakala at 3,397 m. The distance between the two mountains is 150 km.

The velocity range that was used for the analysis and mentioned previously, is 5 to 16 m/s, which is taken as the basis of a typical Hawaiian summer day where the wind velocities between these mountains ranges from 10 to 35 mph. Due to the height of the bacon laser in Mauna Loa, the ambient temperature at that point is 5.5 °C during the daylight varying from a temperature of 15 °C on the sea surface and 25 °C on the base surface of the mountains [19].

Similarly, the variations in pressure are from 101,325 Pa at sea level to 70,630.21 Pa at the height of 3,397 m where the laser emitting device is located.

To carry out my research, I needed to simulate the turbulent behavior of atmospheric conditions among the previously mentioned mountains. Therefore, I needed a CFD simulator and I chose the ANSYS Fluent because of its precision and that it has accurate turbulent flow analysis options. The design process was extensively discussed in Chapter 7 so it will only be mentioned in this chapter as a general summary.

Another big challenge apart from deciding the scaling down the model was to replicate the original conditions of temperature and pressure all over the scaled model. The situation is that in the original geometry, these properties change with the height, then I needed to create a User Defined Function, or UDF, to ensure these variations. The UDF function was used in the inlet, outlet, top, front, and back atmosphere.

Figure 4.2. shows the boundary conditions of pressure, temperature, and velocity in each section, as well the UDF to specify the variation of these properties with respect to height.

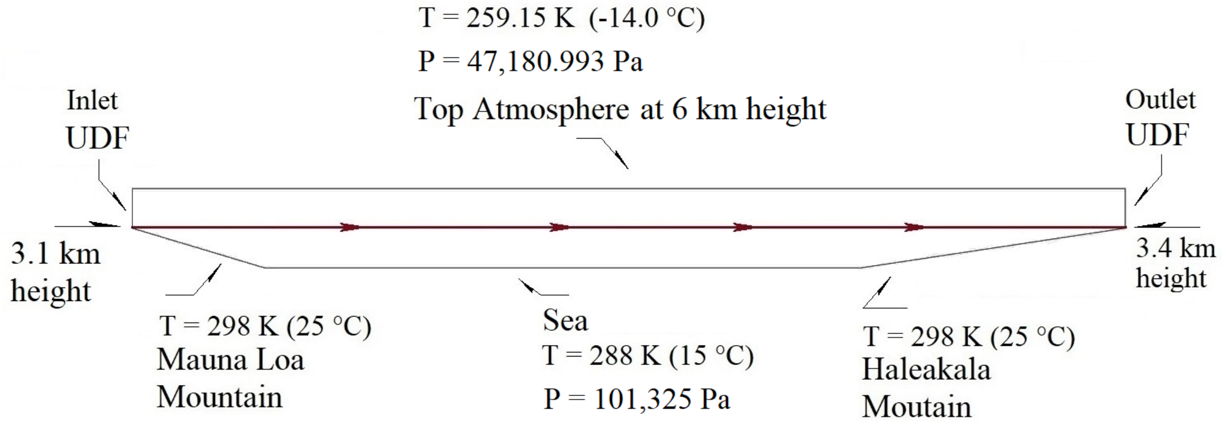

Figure 4.2: Temperature and pressure data in the specified sections.

Equations (4.2) and (4.3) were the ones used to generate the code for the variation of temperatures and pressures.

$$T(h) = 298.15 + 65\,h \tag{4.2}$$

$$P(h) = 101325\,h\,[1 - (2.25577 \times 10^{-5})]^{5.25588} \tag{4.3}$$

Figure 4.3 shows the code in *C* language that was generated with formulas (4.2) and (4.3) to create the UDF that was later uploaded into the *Set up* section of the ANSYS Fluent to run the 45 cases of analysis.

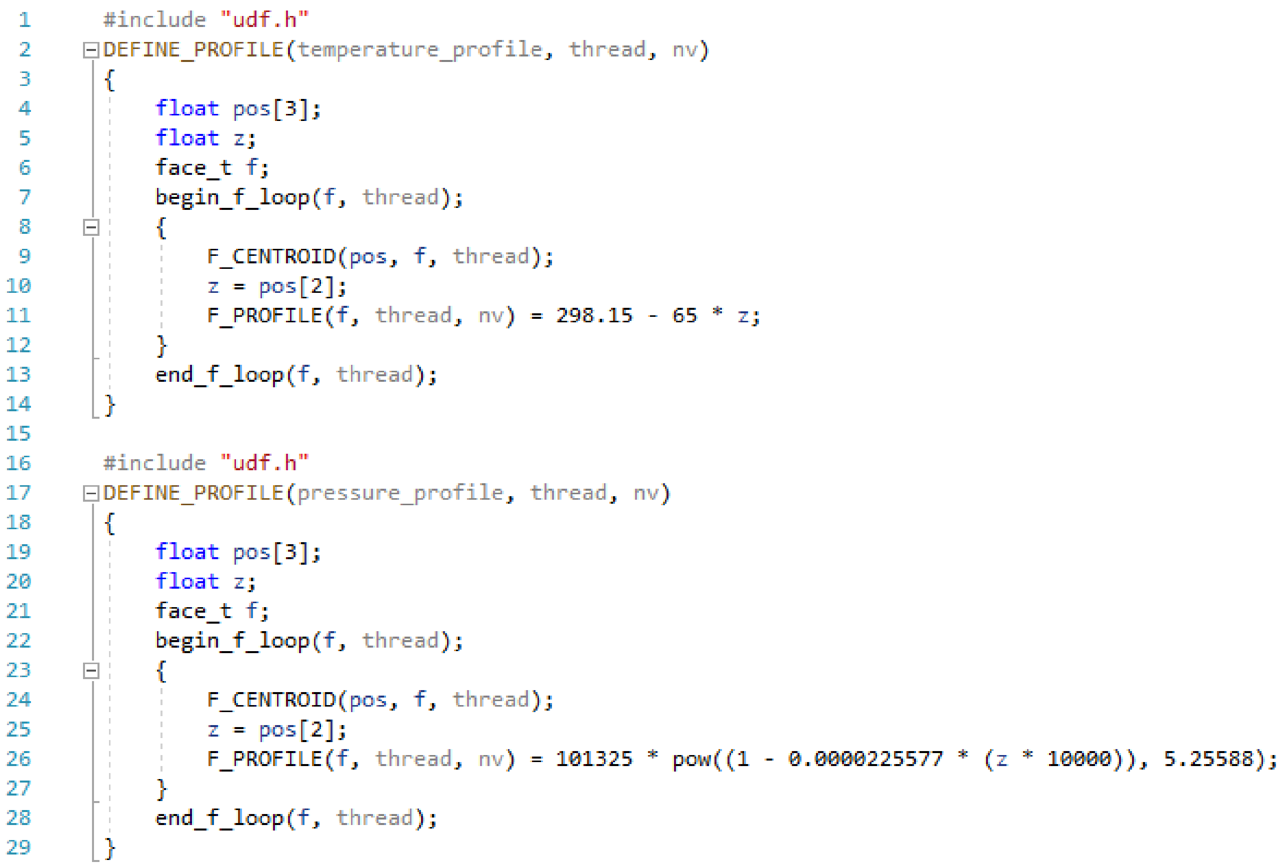

```
#include "udf.h"
DEFINE_PROFILE(temperature_profile, thread, nv)
{
    float pos[3];
    float z;
    face_t f;
    begin_f_loop(f, thread);
    {
        F_CENTROID(pos, f, thread);
        z = pos[2];
        F_PROFILE(f, thread, nv) = 298.15 - 65 * z;
    }
    end_f_loop(f, thread);
}

#include "udf.h"
DEFINE_PROFILE(pressure_profile, thread, nv)
{
    float pos[3];
    float z;
    face_t f;
    begin_f_loop(f, thread);
    {
        F_CENTROID(pos, f, thread);
        z = pos[2];
        F_PROFILE(f, thread, nv) = 101325 * pow((1 - 0.0000225577 * (z * 10000)), 5.25588);
    }
    end_f_loop(f, thread);
}
```

Figure 4.3. Codes to generate the UDF in C language for temperature and pressure.

Analysis. During the analysis stage, the simulation calculations are run in the CFD software which uses the information previously fed. The case of analysis is initialized and subsequently run with a time step size of 0.002 and a number of time steps of 100,000 with a maximum of iterations per time step of 5. In order to handle this high volume of calculations, HPCs (High Performance Computers) is used for solving the cases.

The cases of analysis were generated based on the typical velocity range in this area of Hawaii, where the values have been identified from 10 to 35 mph. Using the conversion to International Units System and with the purpose of using a step size of 0.25 m/s, a range from 5 to 16 m/s was established. Thus, forty-five cases of analysis were defined.

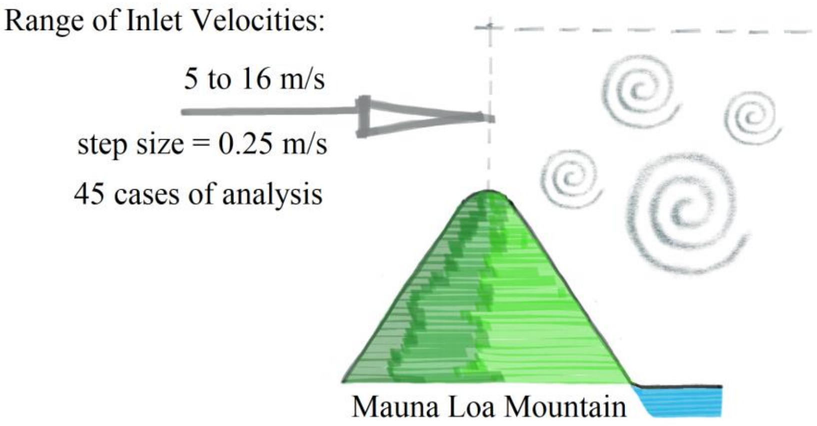

Figure 4.4. Range of velocities for the 45 cases of analysis.

Each case is run in the Fluent section. After this, from the Results section, the data related to velocities, temperatures and pressures over each coordinate is exported and stored into a general .csv file, so it can be used later on other stages of analysis.

The .csv files with the information of coordinates, velocities, temperatures and pressures is defined in non-equidistant coordinates, as it can be seen in the figure 4.5. Thus, it is submitted to a code written in Python language that uses training and prediction tools based on neural algorithms previously defined into *Chapter 2* about the Deep Learning Analysis section.

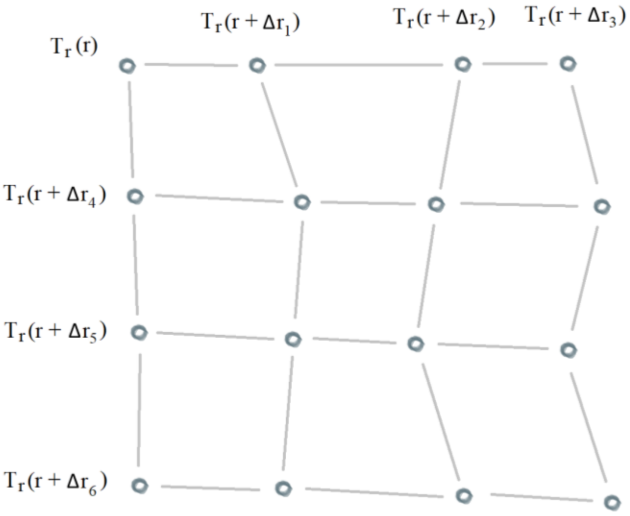

Figure 4.5. Non-equidistant mesh from the ANSYS File.

The neural network algorithm generates a .csv file with the data for velocity, temperature and pressure adjusted to equidistant positions as it can be seen on figure 4.6 [54].

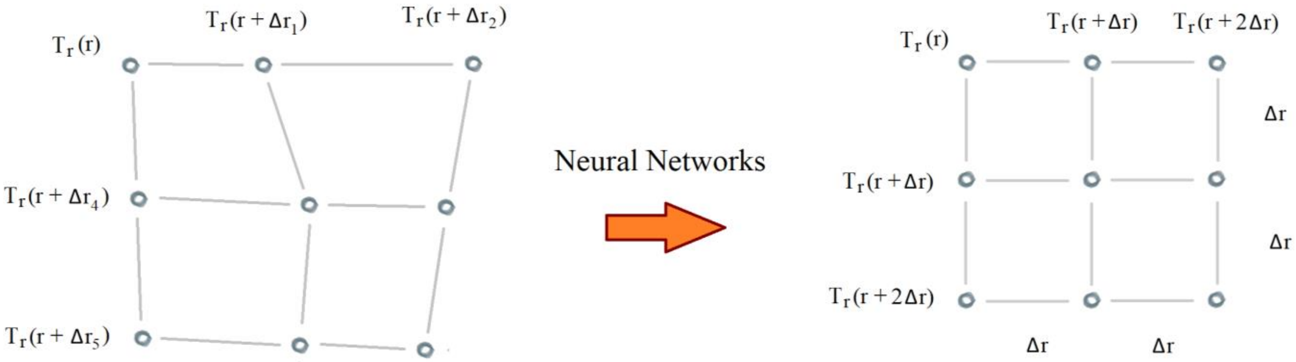

Figure 4.6. Transition from Non-Equidistant to Equidistant Mesh.

The reason of generating equidistant positions is to be able to use the structure function of the temperature which is based on doing the summation of the square difference of the temperatures depending on the position vector r_1 and using a distance r whose value must remain constant during all the summation [11]:

$$D_T = \sum [T_r(r_1 + r) - T_r(r_1)]^2 \tag{4.4}$$

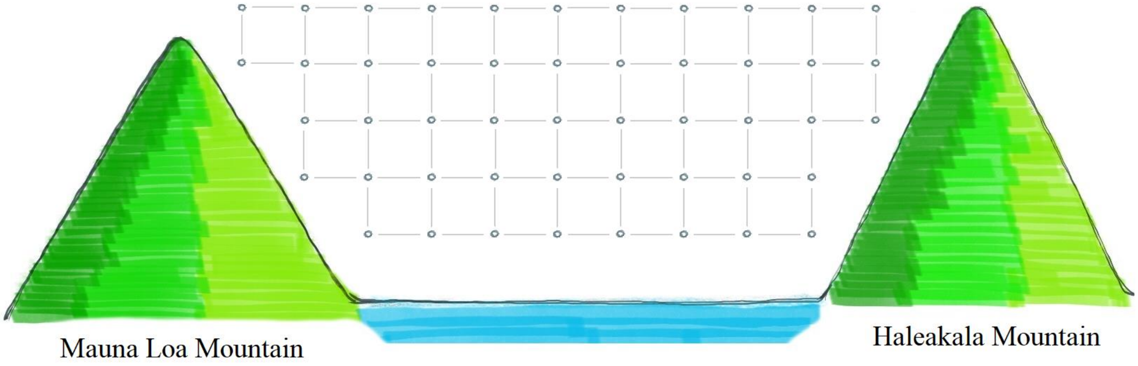

Figure 4.7. Temperature information in equidistant positions.

Once the structural function of temperature has been calculated, the following equations are used to obtain ${C_T}^2$

$$D_T = {C_T}^2 r^{2/3} \tag{4.5}$$

$${C_T}^2 = D_T / r^{2/3} \tag{4.6}$$

The result of the calculations is the structural temperature index C_T^2 and can be considered a universal way of calculating spatial temperature variations. After the C_T^2 was calculated using the python scripts, a new .csv file is created. Thus, the next step is using this information to calculate the refractive index for each case of analysis using the equation (3.6).

$$C_n{}^2 = \left(\frac{79\,P}{T^2} \times 10^{-6}\right)^2 C_T{}^2 \tag{4.7}$$

The values of P and T (Temperature and Pressure) used for the equation, are the characteristic readings at the laser emission point. In the results section, the range of values of $C_n{}^2$ come from these calculations.

Turbulence conditions in open atmosphere begin at a Reynolds number of 5 x 10^5. As previously mentioned, the Reynolds number calculation comes from the equation [20].

$$Re = v\,L/\nu \tag{4.8}$$

The parameters that make up the equation are v, which is the wind velocity in a range from 5 to 16 m/s; L, which is the characteristic dimension of the flow zone, equal to 3 m in the scaled model and ν that is the kinematic viscosity of the air of 1.38×10^{-5} m/s at the temperature of the emission zone which is 5.5 ºC or 278.65 K.

The Figure 10.6 specifies the values of the Reynolds numbers corresponding to the range of velocities from 5 to 16 m/s. This range is from 1.09 x 10^6 to 3.47 x 10^6. Thus, the entire range is above the transition value of 5 x 10^5 that indicates the change from laminar to turbulent flow. Therefore, the entire analyzed phenomenon is at the level of turbulence.

In the methodology section, all the steps that were used to calculate the relation between the Reynolds number and $C_n{}^2$ were shown. It is important to note that once the geometry was generated in a CAD software and the original conditions such as velocity, temperature and pressure were indicated in the boundary conditions of the CFD software, it took time to find a way to place the UDFs (User Defined Functions) into the software to effectively replicate the original conditions of pressure and temperature. One of the members of the research team had used them, he was not available to help on this research, thus I had to focus on doing the investigation of the manuals of ANSYS Fluent, as well as on using the principles of programming in C ++ language. Once these functions were generated, the simulation results were diametrically different from the initial simulations that I was creating showing a series of turbulent conditions that were not observed in the initial simulations [59].

In Chapter 5, I present a series of final series of simulations as well as calculations made for the Reynolds numbers and their corresponding values of the refractive index C_n^2 based on these simulations. Also, a graph that relates both parameters and a calculation of their correlation.

Chapter 5: Results and Discussions.

This Chapter presents the product of all the previous work done with the simulations, algorithmic adjustments, and calculations of the Reynolds numbers, C_T^2 and C_n^2. Before presenting the final sequence of results, I would like to present the intermediate partial results of DT and CT2 in Table 5.1, in which I show the sequence of cases that I run the in ANSYS Fluent to simulate the original conditions. As I mentioned in Chapter 4, the 45 cases were generated by the sequence of velocities from 5 to 16 m/s with a step size of 0.25 m/s. All the cases were run using a mesh size of 20 mm, which generated a total of 450,000 tetrahedral elements and 550,000 nodes.

Boundary conditions. The boundary conditions of temperature and pressure used for the simulations are specified in detail in Chapter 3, with the application of the UDFs (User Defined Functions) to replicate the real profile of temperatures and pressures. All cases were including Energy calculations due to the heat transfer and run as Large Eddie Simulations (LES) under maximum turbulence conditions of 100%. They were run with a time step size of 0.005, and a number of time steps of 50,000 and 5 iterations per time step. This gives a total of 250,000 iterations per case with a total flow time of 1250 seconds.

The initialization values of the cases were set to zero. The cases were run until their 100th iteration in my personal computer and then I exported them to the HPCs (High Performance Computers) to finish running work. Each case was fully completed in 5 days of computational work. Fortunately, 5 cases could be run at a time, so the complete solution of the cases took a total of 45 days of computational work. Once the simulations were finished in the HPCs, the generation of the .csv files was carried out on my personal computer and export the files to the HPCs again to use the neural network algorithms to make the mesh adjusting calculations and later the temperature differentiation for the C_T^2 for which I used python codes. another 10 hours per case, in the same way it was possible to run 5 cases in the HPCs, so all the analysis of D_T in total took 90 hours, for total computational work only related to the structural constant of temperature. Considering the simulations and the calculations of the D_T, the total working time took from the HPCs was about 50 days.

Table 5.1 shows the sequence of velocities corresponding to the Reynolds numbers, which values for calculation are explained on detail in Chapter 4, the D_T, for which most of the computational work for simulating the velocity and temperature profiles was done to calculate it, and the values of C_T^2 and C_n^2. The dispersion of D_T, C_T^2 and C_n^2 values can be observed are a result of temperature variations and will be one of the important points of discussion of this chapter.

Table 5.1: Cases of analysis.

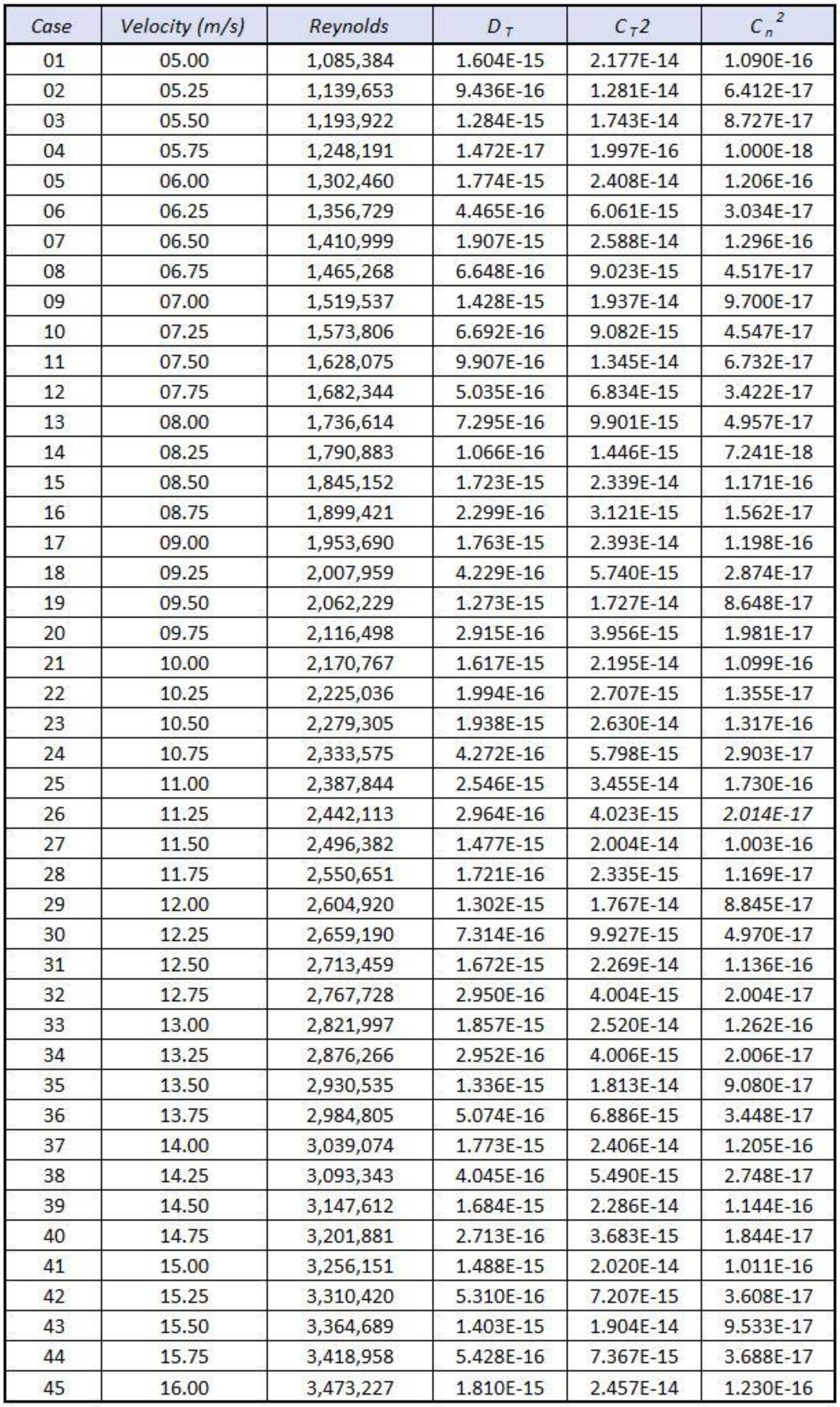

Case	*Velocity (m/s)*	*Reynolds*	D_T	C_T2	C_n^2
01	05.00	1,085,384	1.604E-15	2.177E-14	1.090E-16
02	05.25	1,139,653	9.436E-16	1.281E-14	6.412E-17
03	05.50	1,193,922	1.284E-15	1.743E-14	8.727E-17
04	05.75	1,248,191	1.472E-17	1.997E-16	1.000E-18
05	06.00	1,302,460	1.774E-15	2.408E-14	1.206E-16
06	06.25	1,356,729	4.465E-16	6.061E-15	3.034E-17
07	06.50	1,410,999	1.907E-15	2.588E-14	1.296E-16
08	06.75	1,465,268	6.648E-16	9.023E-15	4.517E-17
09	07.00	1,519,537	1.428E-15	1.937E-14	9.700E-17
10	07.25	1,573,806	6.692E-16	9.082E-15	4.547E-17
11	07.50	1,628,075	9.907E-16	1.345E-14	6.732E-17
12	07.75	1,682,344	5.035E-16	6.834E-15	3.422E-17
13	08.00	1,736,614	7.295E-16	9.901E-15	4.957E-17
14	08.25	1,790,883	1.066E-16	1.446E-15	7.241E-18
15	08.50	1,845,152	1.723E-15	2.339E-14	1.171E-16
16	08.75	1,899,421	2.299E-16	3.121E-15	1.562E-17
17	09.00	1,953,690	1.763E-15	2.393E-14	1.198E-16
18	09.25	2,007,959	4.229E-16	5.740E-15	2.874E-17
19	09.50	2,062,229	1.273E-15	1.727E-14	8.648E-17
20	09.75	2,116,498	2.915E-16	3.956E-15	1.981E-17
21	10.00	2,170,767	1.617E-15	2.195E-14	1.099E-16
22	10.25	2,225,036	1.994E-16	2.707E-15	1.355E-17
23	10.50	2,279,305	1.938E-15	2.630E-14	1.317E-16
24	10.75	2,333,575	4.272E-16	5.798E-15	2.903E-17
25	11.00	2,387,844	2.546E-15	3.455E-14	1.730E-16
26	11.25	2,442,113	2.964E-16	4.023E-15	*2.014E-17*
27	11.50	2,496,382	1.477E-15	2.004E-14	1.003E-16
28	11.75	2,550,651	1.721E-16	2.335E-15	1.169E-17
29	12.00	2,604,920	1.302E-15	1.767E-14	8.845E-17
30	12.25	2,659,190	7.314E-16	9.927E-15	4.970E-17
31	12.50	2,713,459	1.672E-15	2.269E-14	1.136E-16
32	12.75	2,767,728	2.950E-16	4.004E-15	2.004E-17
33	13.00	2,821,997	1.857E-15	2.520E-14	1.262E-16
34	13.25	2,876,266	2.952E-16	4.006E-15	2.006E-17
35	13.50	2,930,535	1.336E-15	1.813E-14	9.080E-17
36	13.75	2,984,805	5.074E-16	6.886E-15	3.448E-17
37	14.00	3,039,074	1.773E-15	2.406E-14	1.205E-16
38	14.25	3,093,343	4.045E-16	5.490E-15	2.748E-17
39	14.50	3,147,612	1.684E-15	2.286E-14	1.144E-16
40	14.75	3,201,881	2.713E-16	3.683E-15	1.844E-17
41	15.00	3,256,151	1.488E-15	2.020E-14	1.011E-16
42	15.25	3,310,420	5.310E-16	7.207E-15	3.608E-17
43	15.50	3,364,689	1.403E-15	1.904E-14	9.533E-17
44	15.75	3,418,958	5.428E-16	7.367E-15	3.688E-17
45	16.00	3,473,227	1.810E-15	2.457E-14	1.230E-16

Next, I present a series of the velocity and temperature simulations to get an idea of the possible results obtained when calculating the relation between the Reynolds number and the C_n^2. Together, Figures 5.1 and 5.2 show the temperature profiles for the full sequence from 5 to 16 m/s respectively, with a step size of 1 m/s. I used the 1 m/s step size in order to use pictures that could cover the entire range of velocities. On the same way, Figures 5.3 and 5.4 together show the entire velocities profiles from 5 to 16 m/s with a step size of 1 m/s for the same reason to cover the entire range of velocities in a series of pictures.

The sequence of the temperature profiles shows mainly strong variations, although there are some cases in which this contrasts are weaker despite the fact that the velocity is increasing with each case, this is the reason why in the later graph 5.1, there is an enormous variability in the values of C_n^2. Despite this variability, this positive trend can be observed between both variables, and whose relation was calculated using the numerical method of least squares for curve fitting that has been coded in Python.

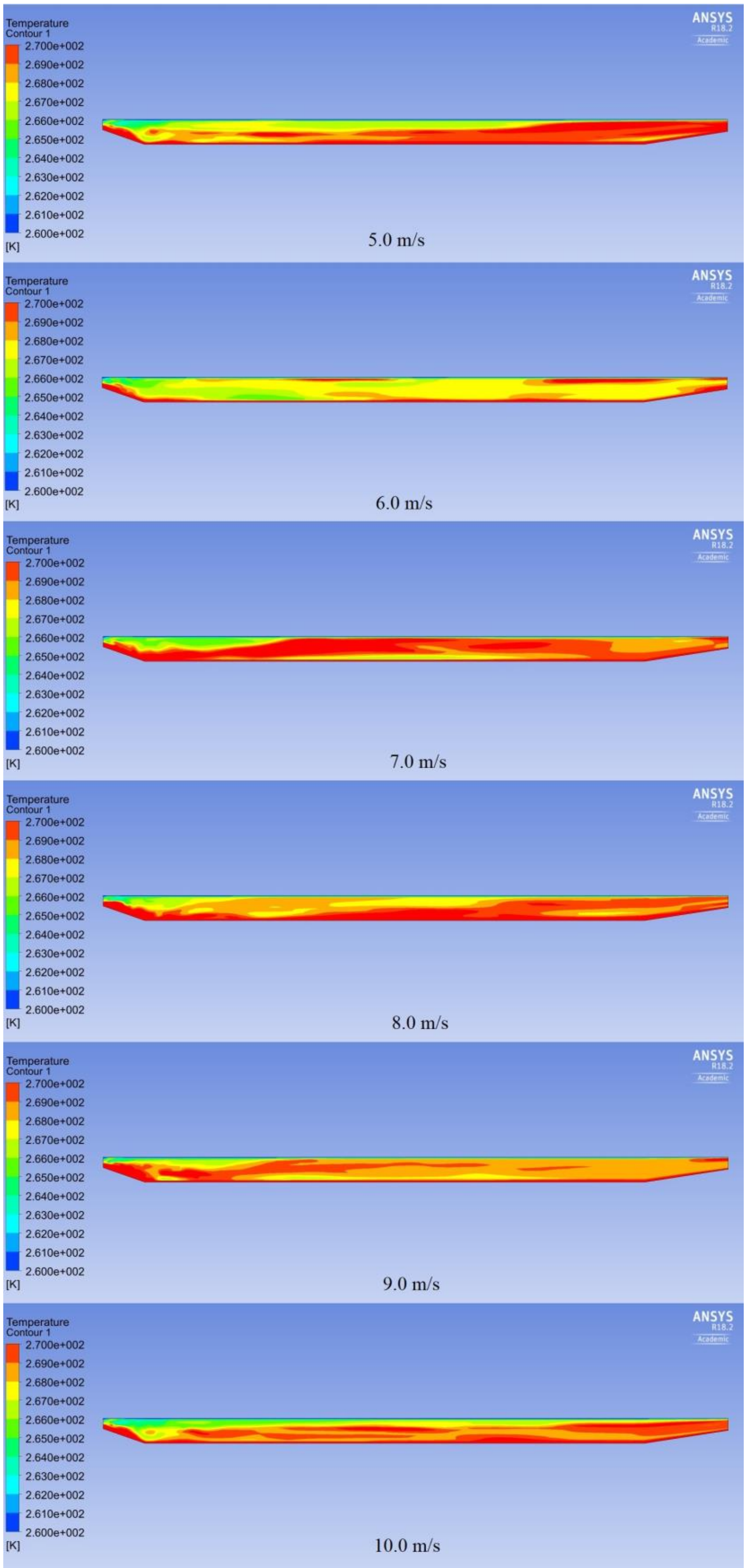

Figure 5.1: Profiles of temperatures at a range of velocities from 5 to 10 m/s.

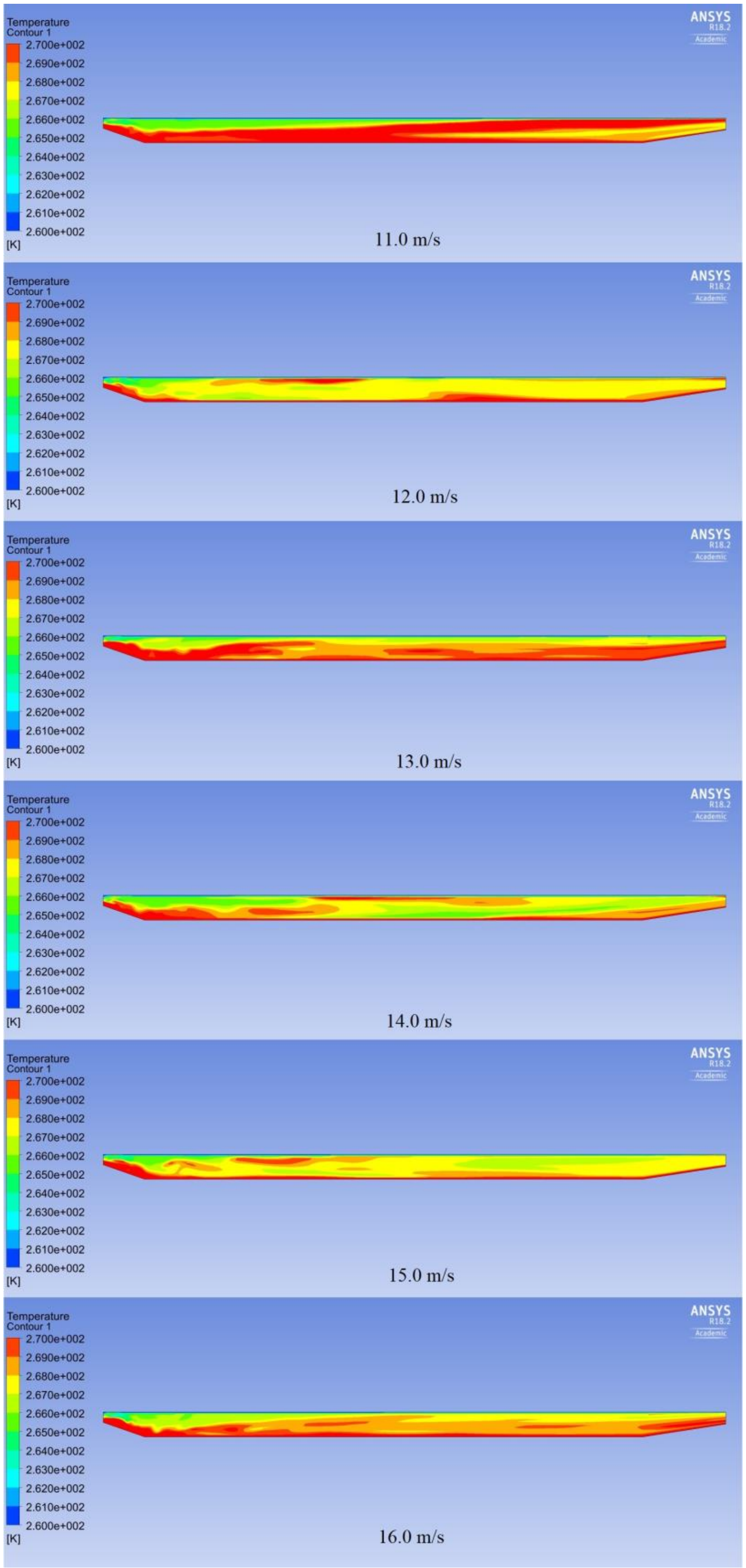

Figure 5.2: Profiles of temperatures at a range of velocities from 11 to 16 m/s.

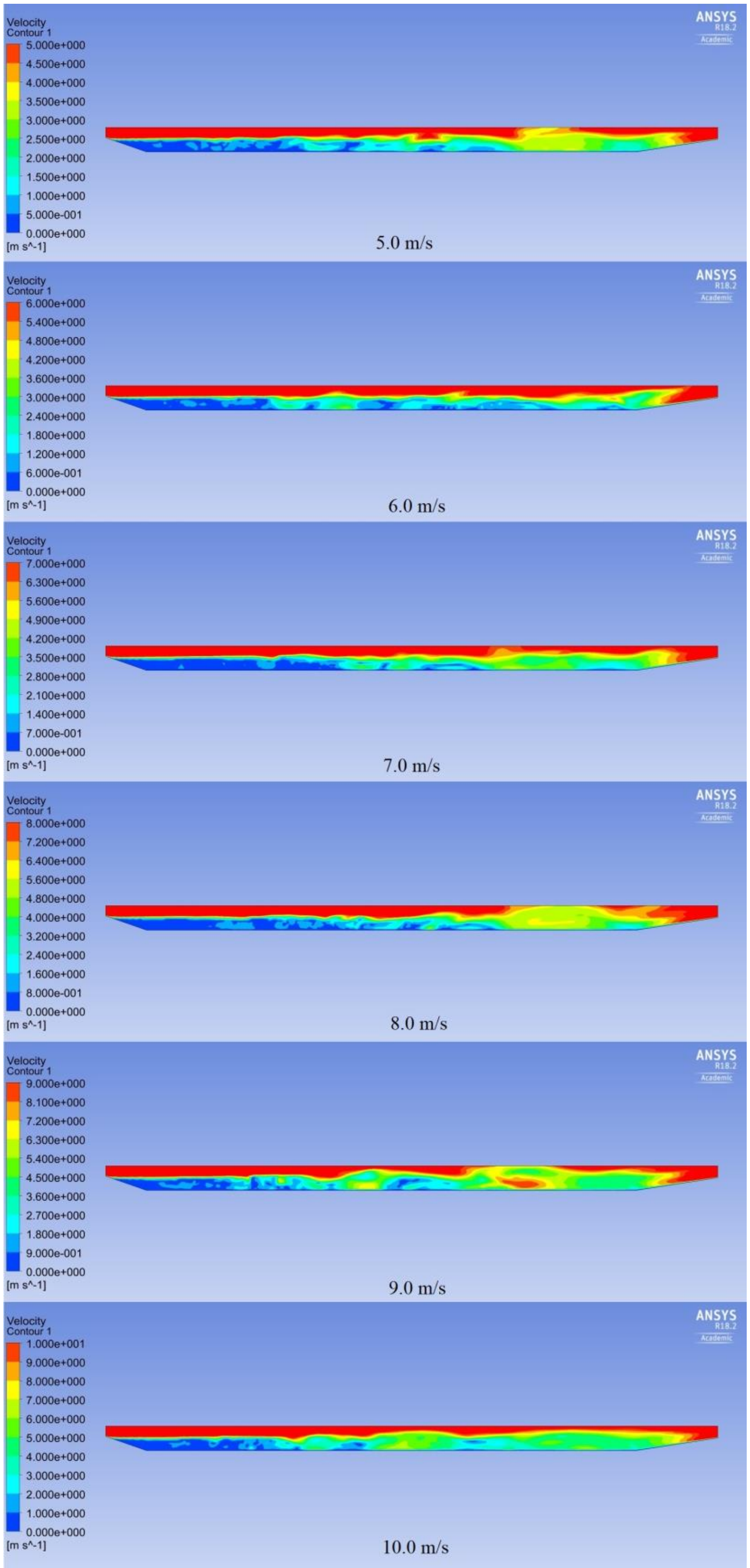

Figure 5.3: Profiles of velocities for a range of velocities from 5 to 10 m/s.

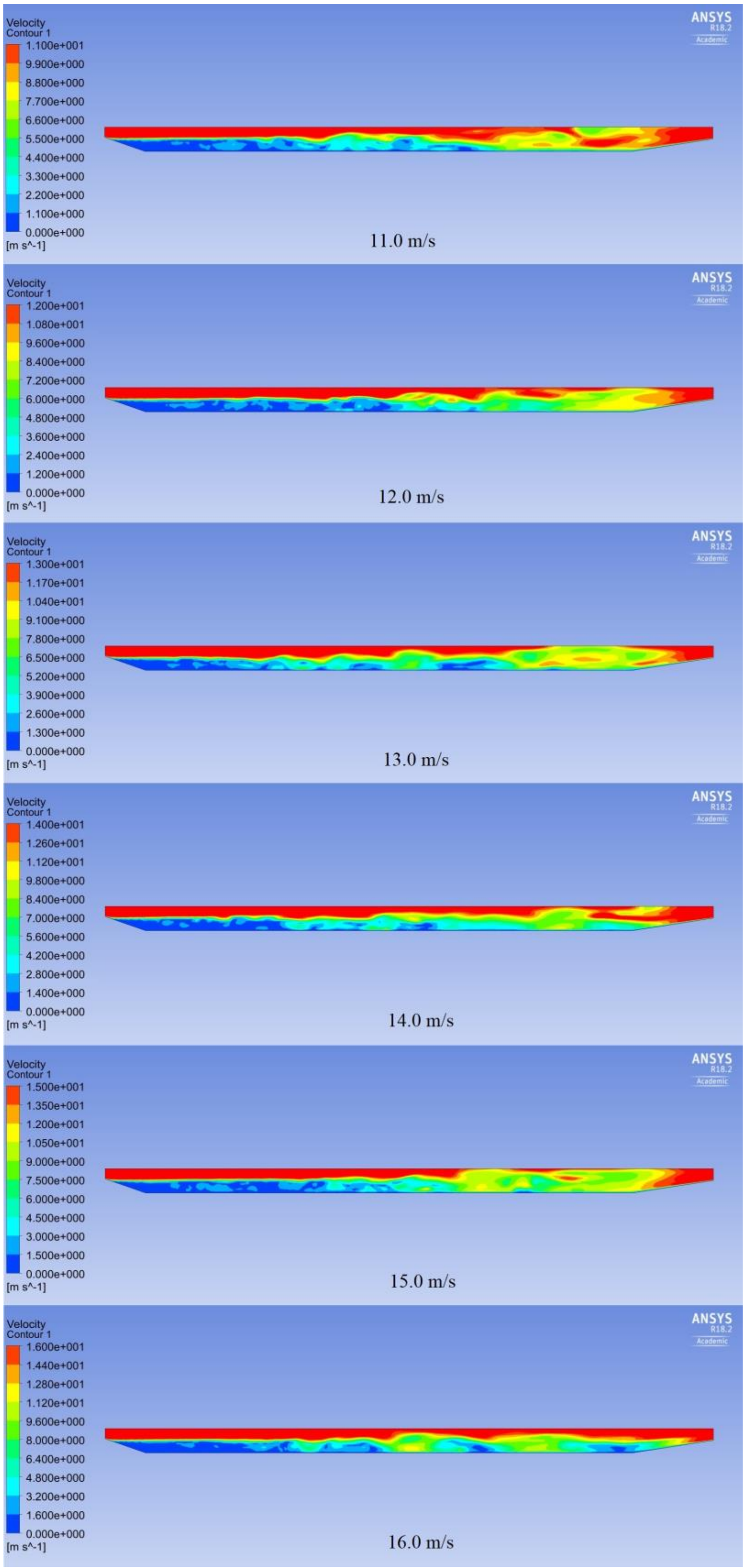

Figure 5.4: Profiles of velocities for a range of velocities from 11 to 16 m/s.

Returning to the theme of variability between each of the cases of the velocity and temperature profiles, it is also notorious to observe that, even within each case, when the number of iterations increases, there are notable variations in the velocity and temperature from the previously set of iterations. This tells us that the turbulence phenomenon, even in cases of mathematical estimation, shows its chaotic nature.

It is also important to note that by drawing a line between the tops of the mountains, just over the lasers' path, it is observed that this part of the geometry experiences the greatest variations in temperature and velocity, since the wind that passes over the laboratories experiences a sudden drop on the orographic conditions, drastically changing the height, and with it, the velocity and temperature. The inverse phenomenon happens when the wind flow passes over the second laboratory, decreasing the height and changing the properties of the wind.

Additionally, as seen in Figures 5.3 and 5.4, the behavior of the velocity is approximately uniform in the first half of the geometry but, especially in the range of highest velocities from 11 to 16 m/s, the friction that the air flow has on the surface of the mountains as well as over the sea, tends to make their effects on the flow showing zones of high level of turbulence, with the formation of zones of high rotation with an approximate diameter measurement of 2 kms.

Table 5.2: Reynolds vs C_n^2

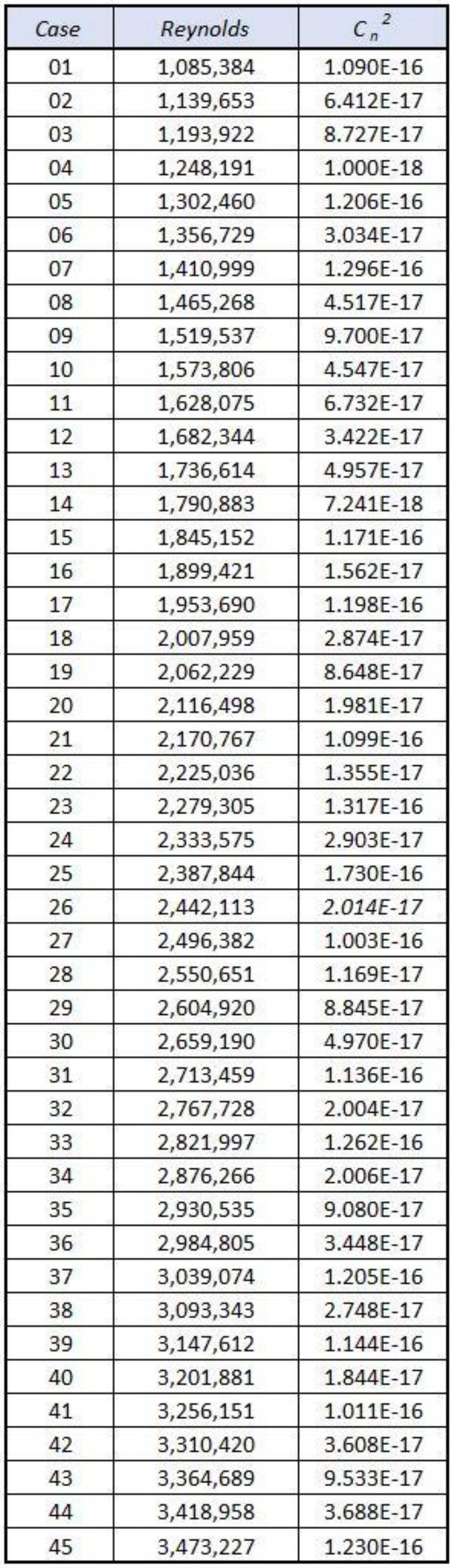

Case	*Reynolds*	C_n^2
01	1,085,384	1.090E-16
02	1,139,653	6.412E-17
03	1,193,922	8.727E-17
04	1,248,191	1.000E-18
05	1,302,460	1.206E-16
06	1,356,729	3.034E-17
07	1,410,999	1.296E-16
08	1,465,268	4.517E-17
09	1,519,537	9.700E-17
10	1,573,806	4.547E-17
11	1,628,075	6.732E-17
12	1,682,344	3.422E-17
13	1,736,614	4.957E-17
14	1,790,883	7.241E-18
15	1,845,152	1.171E-16
16	1,899,421	1.562E-17
17	1,953,690	1.198E-16
18	2,007,959	2.874E-17
19	2,062,229	8.648E-17
20	2,116,498	1.981E-17
21	2,170,767	1.099E-16
22	2,225,036	1.355E-17
23	2,279,305	1.317E-16
24	2,333,575	2.903E-17
25	2,387,844	1.730E-16
26	2,442,113	*2.014E-17*
27	2,496,382	1.003E-16
28	2,550,651	1.169E-17
29	2,604,920	8.845E-17
30	2,659,190	4.970E-17
31	2,713,459	1.136E-16
32	2,767,728	2.004E-17
33	2,821,997	1.262E-16
34	2,876,266	2.006E-17
35	2,930,535	9.080E-17
36	2,984,805	3.448E-17
37	3,039,074	1.205E-16
38	3,093,343	2.748E-17
39	3,147,612	1.144E-16
40	3,201,881	1.844E-17
41	3,256,151	1.011E-16
42	3,310,420	3.608E-17
43	3,364,689	9.533E-17
44	3,418,958	3.688E-17
45	3,473,227	1.230E-16

As a result of the velocity and temperature profiles, as well as the C_T^2 and C_n^2 calculations, the Table 5.5 was constructed. In this table, a similar variability of the temperature differences showed in the temperature profiles can be observed in the variability of C_n^2. From Table 5.1, Figure 5.5 was constructed, which shows the behavior of the Reynolds number and the C_n^2.

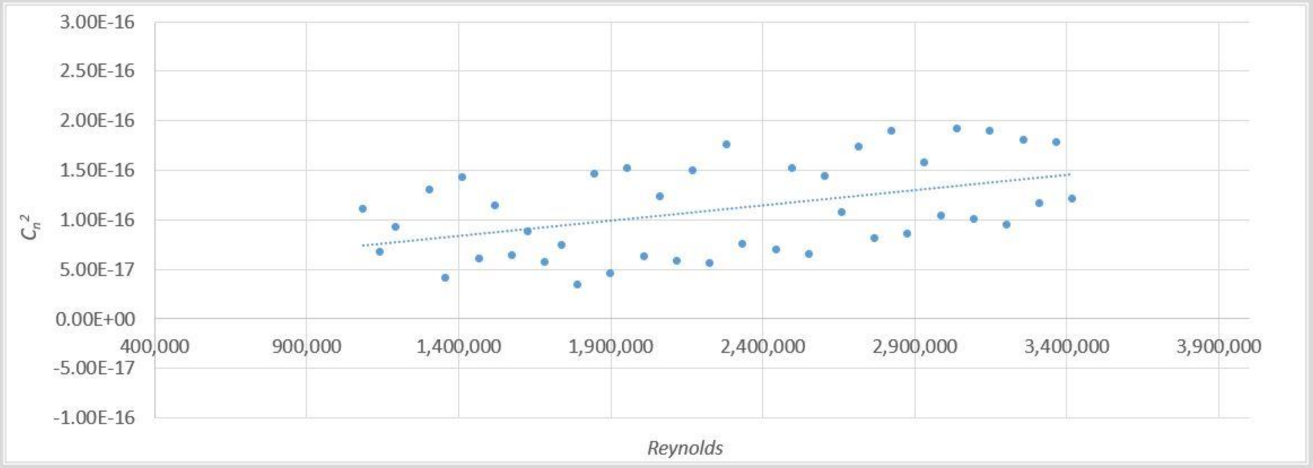

Figure 5.5: C_n^2 vs *Re* trend.

The equation (5.1) describes the trend of C_n^2 with respect to the Reynolds number.

$$C_n{}^2 = 3 \times 10^{-23} Re + 4 \times 10^{-17} \tag{5.1}$$

An extremely important point to highlight is that the cases 13 and 25 were eliminated from the graph because the resultant C_n^2 values corresponding to each case showed atypical behavior. The case 13 that has a velocity of 8.00 m/s generated a C_n^2 of 4.96 x 10^{-17}, this value very close to 0, so I decided to eliminate it. For the case 25, that has a velocity of 11 m/s, and a corresponding C_n^2 of 1.73 x 10^{-16}; this a value very far away from the rest of the C_n^2 values, so I also decided to eliminate it. The probable reason for these atypical values is, from one part, the lack of sufficient elements in the ANSYS Fluent due to the use of a student license and, from another part, there are probably zones of thermal variation in the real geometry that are not able to be simulated with CFD software due to the use of the UDFs (User Defined Functions) that follow strict equations.

The positive relation between the Reynolds number and the C_n^2 can be seen from the diagram and from the equation. It is a positive linear trend with a noticeable dispersion. When analyzing the graph, the size of this dispersion as well as certain patterns get the attention [19]. This could be explained on the base that the temperature values in a state of turbulence, show a lot of variations due to the chaotic nature of the phenomenon. At this time, it is worth presenting again the figure that was used in Chapter 2 about the theoretical background of this thesis in order to make a comparison of the dispersion of C_n^2 values.

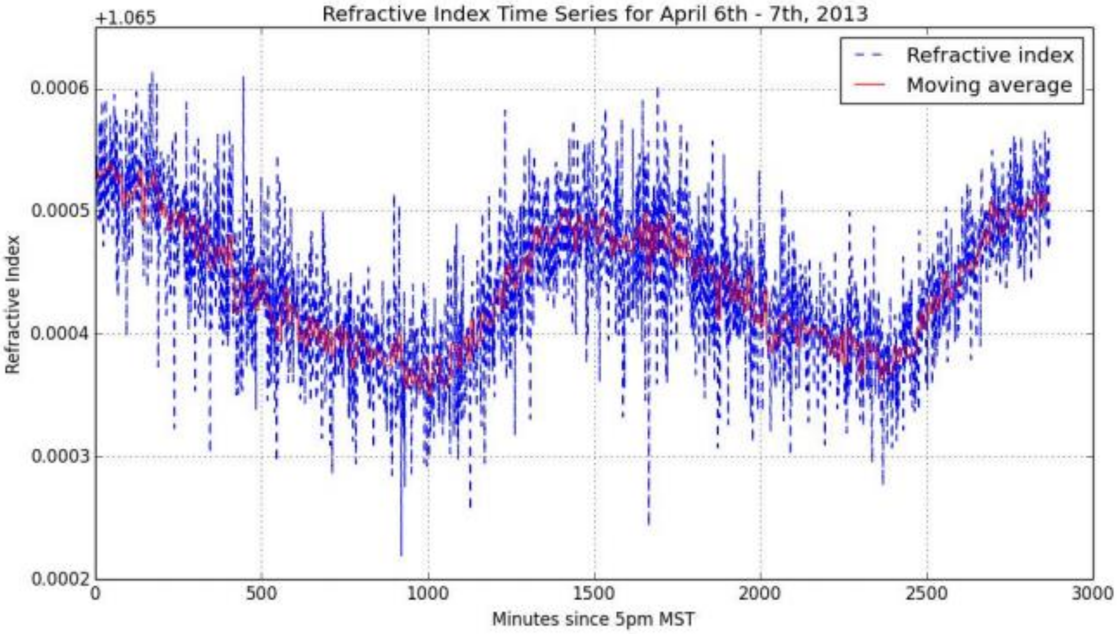

Figure 5.6: Distribution of the Cn value during a typical spring day in Hawaii.

Figure 5.6 shows the enormous *n-1 (refractive index)* variation that the parameter experiences per minute and yet the trend per section is clear. The values presented in Figure 5.5 are average values of the temperature variations at a certain time of day with the entire range of the 45 cases run for the velocity range of 5 to 16 m/s.

On the other hand, the Figure 5.5 is made on the basis of experimental readings, and 5.1 is based on CFD simulation, so that a notable similarity can be observed in the variations of the values for both behaviors: experimental vs simulated. Nevertheless, the trend is clearly observed, for this reason I consider this estimation good enough for understanding the relation between the Reynolds number and the C_n^2.

Correlation between Re and C_n^2. Based on Table 5.2, the degree of correlation between Reynolds number Re and Refractive index C_n^2 has been calculated. The value obtained is the correlation coefficient r = 0.511, where r is a sample correlation coefficient. The range of the correlation coefficient is from -1 to 1. So, the result of the correlation coefficient r = 0.511 or 51.10% indicated that the variables *Re* and C_n^2 have a moderate positive correlation [57], meaning that they are likely to move in the same direction.

These values reinforce the initial objective of finding a relation between the two variables that would allow predicting, above all, the value of C_n^2 with the Reynolds values as well as obtaining a mathematical relation between the two variables [60].

It should be noted that, an r value that would suggest a strong positive relationship between the two variables is larger than 0.7. Nonetheless, a potent point is, with a large number of elements (population data) and a professional ANSYS Fluent license that can accommodate much larger data size, the simulations could lead us to a larger r value. Where, r is the population correlation coefficient.

Chapter 6: Conclusions.

The objective of the equation that relates the Reynolds number and the structure refractive index constant C_n^2 is to represents an adequate platform for those who adjust the laser communication systems in the Mauna laboratory. Based on this equation, the idea is that they program automatic adjustments directly related to the instantaneous wind velocity at their location.

An important point to consider is that there is a noticeable dispersion of the C_n^2 values as the Reynolds number values vary. This variation can be explained in that the turbulence phenomenon is chaotic and trying to simulate it using CFD software presents high levels of variability. It is important to comment that the adjustments have not been tested in optical communication elements, and that the equation that defines the trend between the optical diffraction constant and the Reynolds number are based on a temperature scale at a typical value of 25 °C at sea level, reason why the equation must be valid in these conditions.

In Chapter 3 it was presented how even when simulating the initial conditions of velocity, the temperature show considerable variability as the number of iterations continue to grow even though each case was considered in a fully developed condition. For this reason, when I identified the conditions of variability of C_n^2, that depend directly on the temperature variations, I gave them less importance when I identified the positive trend of C_n^2 as the values of the Reynolds number varied. This is because, although the dispersion of values is appreciated, the trend is clearly defined even visually.

The use of a software platform such as the ANSYS Fluent, whose operation is based on the Navier-Stokes equations, represents an extremely useful tool to generate the profile of temperatures and velocities at different positions in the space at a given time, however, the necessary scaling of the model, represents a weakness that affects the accuracy of the predictions. Additionally, the inaccuracy of the spatial positions in the sensitive mesh that CFD models create, despite having internal adjusting tools, requires the use of additional computational scripts to generate the required proportional spaces for analyzing the data. This is where Neural Network algorithms, with their training and prediction steps, come with high accuracy to solve this need, as they are able to use data on the basis of a non-equidistant mesh to be trained and then predict a series of data on the basis of an equidistant mesh.

Finally, it can be said that the use of the Python programming platform was decisive in order to use all the data collected from our CFD Simulator (ANSYS Fluent), encode the neural network algorithms and work on the data obtained from this codification to perform the calculations of C_T^2 and C_n^2 in order to obtain the equation that relates Reynolds vs C_n^2.

I would like to acknowledge the U.S. Department of Defense (AFOSR Grant Number # FA9550-19-1-0304, FA9550-17-1-0253, FA9550-12-1-0242, FA9550-17-1-0393, SFFP, AFTC, HAFB/HSTT, AFRL, HPCMP), Department of Energy (DE-FE0026220, DE-FE0002407, NETL, Sandia, ORNL, NREL), Systems Plus, and several other individuals at these agencies for partially supporting our research financially or through mentorship. We would also like to thank NSF ((HRD-1139929, XSEDE Award Number ACI-1053575), TACC, DOE, DOD HPCMP, University of Texas STAR program, UTEP (Research Cloud, Department of Mechanical Engineering, Graduate School & College of Engineering) for generously providing financial support or computational resources. Without their generous support it would have been almost impossible to complete the milestones.

Chapter 7: Future Studies.

In this chapter, the elements that were missing in the present study are identified, either due to lack of information, limitations on resources, or the need of more time to delve into other aspects of the research.

An important aspect to consider is having experimental data of velocities, temperatures, and pressures in order to make a comparison that would allow corrections and identify more improvement points. It is possible that the laboratories at Maui may have this information, so you it is important to make contact them for this information to be shared.

Additionally, as it is discussed during the study, the ANSYS Fluent license that was used during the simulation of the turbulence conditions was a student one, which had the limitation in the number of 500,000 elements to carry out the simulation. A professional license must have access to a considerably greater number of elements so that the turbulence phenomenon can be simulated with much more accuracy.

It would be worth verifying if, by increasing the capacity of elements in the simulation, the dispersion of the C_n^2 values continues to have the variability presented in this study, or the correlation between both variables increases.

It is important to comment that for the generation of experimental data there is also the possibility to obtain experimental using a wind tunnel. It could allow obtaining readings that would help to make comparisons with the data generated with the CFD.

The present analysis was performed on the basis of an ambient temperature scale based on a set point of 25 Celsius on daylight and a range of maximum wind velocities, however, future work may also include a range of average velocities as well as a range of nighttime ambient temperatures to know the behavior of C_n^2 at night.

It will also be worth considering the effect of turbulence on optical variables such as Fried coherence length, isoplanatic angle, spectra of figure and tilt and several other optical parameters and use this information to develop analytical expressions.

The Fried coherence length measures the quality of the laser transmission trough the atmosphere due to random inhomogeneities in the refractive index, mainly as variations of temperature, and in consequence in density.

Since the equation that defines the trend between the optical diffraction constant and the Reynolds number are based on a temperature scale at a typical value of 25 °C at sea level, thus a future point of analysis is to carry out the same calculations but varying the initial temperatures in the ground so that all the temperature ranges during the day are included on this study and not just a typical value.

Scholarly contributions

[1] Rodriguez, A., Kotteda, V. M. Krushnarao, Rodriguez, L.F., Kumar, V., Schiaffino, A., Nieto, Z. R. "Machine Learning Approach to Predict the Flow Rate for an Immiscible Two-Phase Flow at Pore Scale for Enhanced Oil Recovery Application." Proceedings of the ASME 2018 5th Joint US-European Fluids Engineering Division Summer Meeting. . Montreal, Quebec, Canada. July 15–20, 2018.

[2] Rodriguez, L.F., Kumar, V., Espiritu, J., Bronson, A., Kotteda, V.M., Lozano, D., Rodriguez, A. "Branch and Bound Analysis to Characterize Phase Variations in Laser Propagation Through Deep Turbulence", Proceedings of the ASME-JSME-KSME 2019 Joint Fluids Engineering Conference AJKFLUIDS2019 July 28-August 1, 2019, San Francisco, CA, USA

[3] Rodriguez, L. F., Vinod, K., Rodriguez, A., Kotteda, V.M.K., Gudimetla, V.S., Munoz, J.A., "Parameter Sensitivity and Statistical Correlation Found in Atmospheric Turbulence Studies" Proceedings of the ASME 2020 Fluids Engineering Division Summer Meeting FEDSM2020 July 12-16, 2020, Orlando, Florida, USA

[4] Rodriguez, A., Vinod, K., Rodriguez, L.F., Kotteda, V.M.K., Gudimetla, V.S., Munoz, J.A., "Stochastic Analysis of Large Eddie Simulations Atmospheric Turbulence Solutions with Generative Machine Learning Models" Proceedings of the ASME 2020 Fluids Engineering Division Summer Meeting FEDSM2020 July 12-16, 2020, Orlando, Florida, USA

[5] Rodriguez, A., Vinod, K., Rodriguez, L.F., Kotteda, V.M.K., Gudimetla, V.S., Munoz, J.A., “Trilinos Solvers Scalability on a MFIX-Trilinos Framework Applied to Fluidized Bed

Simulations" Proceedings of the ASME 2020 Fluids Engineering Division Summer Meeting FEDSM2020 July 12-16, 2020, Orlando, Florida, USA

[6] Rodriguez, L. F., Vinod, K., Gudimetla, R., Munoz, J.A."Machine Learning Analysis to Characterize Phase Variations in Laser Propagation Through Deep Turbulente". May 2020. ASME Journal of Fluids Engineering. [FE-20-1335 UNDER REVIEW]

References

[1] M. Vorontsov *et al.*, “Comparison of turbulence-induced scintillations for multi-wavelength laser beacons over tactical (7 km) and long (149 km) atmospheric propagation paths,” Sep. 2011.

[2] M. A. Vorontsov *et al.*, “Characterization of atmospheric turbulence effects over 149 km propagation path using multi-wavelength laser beacons,” AIR FORCE RESEARCH LAB KIHEI MAUI HI DETACHMENT 15, 2010.

[3] A. M. Abdilghanie, L. R. Collins, and D. A. Caughey, “Comparison of turbulence modeling strategies for indoor flows,” *J. Fluids Eng.*, vol. 131, no. 5, 2009.

[4] V. Markov, A. Khizhnyak, D. Woll, J. Trolinger, and F. Eaton, “Optical phase conjugation for atmospheric turbulence assessment,” in *Atmospheric Propagation III*, 2006, vol. 6215, p. 62150J.

[5] V. I. Tatarskii, “The effects of the turbulent atmosphere on wave propagation,” *Jerusalem Isr. Progr. Sci. Transl. 1971*, 1971.

[6] S. F. Clifford, “The classical theory of wave propagation in a turbulent medium,” in *Laser beam propagation in the atmosphere*, Springer, 1978, pp. 9–43.

[7] J. R. Kerr, “Experiments on turbulence characteristics and multiwavelength scintillation phenomena,” *JOSA*, vol. 62, no. 9, pp. 1040–1049, 1972.

[8] A. Consortini, F. Cochetti, J. H. Churnside, and R. J. Hill, “Inner-scale effect on irradiance variance measured for weak-to-strong atmospheric scintillation,” *JOSA A*, vol. 10, no. 11, pp. 2354–2362, 1993.

[9] H. Yuksel, J. Harris, Y. Tang, R. Gammon, and C. Davis, “Aperture averaging and

correlation function measurements in strong atmospheric turbulence for optical wireless applications," in *Free-Space Laser Communications VIII*, 2008, vol. 7091, p. 70910N.

[10] R. L. Phillips and L. C. Andrews, "Measured statistics of laser-light scattering in atmospheric turbulence," *JOSA*, vol. 71, no. 12, pp. 1440–1445, 1981.

[11] S. K. Friedlander and L. Topper, *Turbulence: classic papers on statistical theory*. Interscience Publishers, 1961.

[12] T. C. Rebollo and R. Lewandowski, *Mathematical and numerical foundations of turbulence models and applications*. Springer, 2014.

[13] J. D. Anderson and J. Wendt, "Computational Fluid Dynamics, Vol. 206, 332." New York: McGraw-Hill, 1995.

[14] A. Zilberman, E. Golbraikh, and N. S. Kopeika, "Propagation of electromagnetic waves in Kolmogorov and non-Kolmogorov atmospheric turbulence: three-layer altitude model," *Appl. Opt.*, vol. 47, no. 34, pp. 6385–6391, 2008.

[15] C. M. White and M. G. Mungal, "Mechanics and prediction of turbulent drag reduction with polymer additives," *Annu. Rev. Fluid Mech.*, vol. 40, pp. 235–256, 2008.

[16] J. P. Bos, M. C. Roggemann, and V. S. R. Gudimetla, "Anisotropic non-Kolmogorov turbulence phase screens with variable orientation," *Appl. Opt.*, vol. 54, no. 8, pp. 2039–2045, 2015.

[17] V. S. R. Gudimetla, R. B. Holmes, and J. F. Riker, "Analytical expressions for the log-amplitude correlation function for plane wave propagation in anisotropic non-Kolmogorov refractive turbulence," *JOSA A*, vol. 29, no. 12, pp. 2622–2627, 2012.

[18] D. Dayton, B. Pierson, B. Spielbusch, and J. Gonglewski, "Atmospheric structure function measurements with a Shack–Hartmann wave-front sensor," *Opt. Lett.*, vol. 17, no. 24, pp.

1737–1739, 1992.

[19] R. Gudimetla, “Estimating Cn2 (Refractive index structure constant) in Deep Turbulence using Unwrapped Phase,” in *Propagation Through and Characterization of Distributed Volume Turbulence*, 2013, pp. PTu2F-1.

[20] B. E. Stribling, B. M. Welsh, and M. C. Roggemann, “Optical propagation in non-Kolmogorov atmospheric turbulence,” in *Atmospheric Propagation and Remote Sensing IV*, 1995, vol. 2471, pp. 181–196.

[21] G. Weiss, “Wave Propagation in a Turbulent Medium. VI Tatarski. Translated by RA Silverman. McGraw-Hill, New York, 1961. 285 pp. Illus. $9.75.” American Association for the Advancement of Science, 1961.

[22] P. S. Bernard and J. M. Wallace, *Turbulent flow: analysis, measurement, and prediction*. John Wiley & Sons, 2002.

[23] F. G. Schmitt, “About Boussinesq’s turbulent viscosity hypothesis: historical remarks and a direct evaluation of its validity,” *Comptes Rendus Mécanique*, vol. 335, no. 9–10, pp. 617–627, 2007.

[24] J. W. Strohbehn, “Line-of-sight wave propagation through the turbulent atmosphere,” *Proc. IEEE*, vol. 56, no. 8, pp. 1301–1318, 1968.

[25] J. C. Vassilicos, “Dissipation in turbulent flows,” *Annu. Rev. Fluid Mech.*, vol. 47, pp. 95–114, 2015.

[26] M. Tsubokura, “Subgrid Scale Modeling of Turbulence for the Dynamic Procedure Using FDM and Its Assessment on the Thermally Stratified Turbulent Channel Flow,” in *ASME/JSME 2003 4th Joint Fluids Summer Engineering Conference*, 2003, pp. 2033–2041.

[27] L. C. Andrews and R. L. Phillips, “Laser beam propagation through random media,” 2005.

[28] T. J. Ypma, “Historical development of the Newton–Raphson method,” *SIAM Rev.*, vol. 37, no. 4, pp. 531–551, 1995.

[29] A. Quirrenbach, “The development of astronomical interferometry,” *Exp. Astron.*, vol. 26, no. 1–3, pp. 49–63, 2009.

[30] L. A. Chernov and R. A. Silverman, *Wave propagation in a random medium*. McGraw-Hill New York, 1960.

[31] F. Ducros, F. Nicoud, and T. Poinsot, “Wall-adapting local eddy-viscosity models for simulations in complex geometries,” *Numer. Methods Fluid Dyn. VI*, pp. 293–299, 1998.

[32] J. Schmidt, “Numerical simulation of optical wave propagation with examples in MATLAB,” 2010.

[33] M. S. Shadloo and M. Yildiz, “Numerical modeling of Kelvin–Helmholtz instability using smoothed particle hydrodynamics,” *Int. J. Numer. Methods Eng.*, vol. 87, no. 10, pp. 988–1006, 2011.

[34] D. L. Walters and D. K. Miller, “Evolution of an upper-tropospheric turbulence event—comparison of observations to numerical simulations,” in *Preprints, 13th Symposium on Boundary Layer Turbulence*, 1999, pp. 157–160.

[35] E. Vilar and J. Haddon, “Measurement and modeling of scintillation intensity to estimate turbulence parameters in an earth-space path,” *IEEE Trans. Antennas Propag.*, vol. 32, no. 4, pp. 340–346, 1984.

[36] F. H. Harlow and J. E. Welch, “Numerical calculation of time-dependent viscous incompressible flow of fluid with free surface,” *Phys. fluids*, vol. 8, no. 12, pp. 2182–2189, 1965.

[37] D. A. L. Jimenez, “Implementing Large Eddy Simulation to Numerical Simulation of Optical Wave Propagation,” 2018.

[38] J. M. McDonough, “Lectures in elementary fluid dynamics: physics, mathematics and applications,” 2009.

[39] Y. Mizuno, T. Yagi, and K. Mori, “Contribution of attached eddies to the intensity and turbulent transfer of velocity fluctuations in wall-turbulence,” *Fluid Dyn. Res.*, vol. 50, no. 4, p. 45513, 2018.

[40] T. DalBello, V. Dippold III, and N. J. Georgiadis, “Computational study of separating flow in a planar subsonic diffuser,” 2005.

[41] P. G. Baines and H. Mitsudera, “On the mechanism of shear flow instabilities,” *J. Fluid Mech.*, vol. 276, pp. 327–342, 1994.

[42] J. Schmidhuber, “Deep learning in neural networks: An overview,” *Neural networks*, vol. 61, pp. 85–117, 2015.

[43] Y. LeCun, Y. Bengio, and G. Hinton, “Deep learning,” *Nature*, vol. 521, no. 7553, pp. 436–444, 2015.

[44] H. Cui, H. Zhang, G. R. Ganger, P. B. Gibbons, and E. P. Xing, “Geeps: Scalable deep learning on distributed gpus with a gpu-specialized parameter server,” in *Proceedings of the Eleventh European Conference on Computer Systems*, 2016, pp. 1–16.

[45] T. Chen *et al.*, “Mxnet: A flexible and efficient machine learning library for heterogeneous distributed systems,” *arXiv Prepr. arXiv1512.01274*, 2015.

[46] M. Kubat, I. Bratko, and R. S. Michalski, “A review of machine learning methods,” *Mach. Learn. Data Min. Methods Appl.*, pp. 3–69, 1998.

[47] M. Abadi *et al.*, “Tensorflow: Large-scale machine learning on heterogeneous distributed

systems," *arXiv Prepr. arXiv1603.04467*, 2016.

[48] A. Odena, V. Dumoulin, and C. Olah, "Deconvolution and checkerboard artifacts," *Distill*, vol. 1, no. 10, p. e3, 2016.

[49] A. Miettinen and T. Siikonen, "Application of pressure-and density-based methods for different flow speeds," *Int. J. Numer. Methods Fluids*, vol. 79, no. 5, pp. 243–267, 2015.

[50] A. D. Wheelon, *Electromagnetic Scintillation: Volume 1, Geometrical Optics*. Cambridge University Press, 2001.

[51] R. I. Emori and D. J. Schuring, *Scale models in engineering: Fundamentals and applications*. Elsevier, 2016.

[52] V. Heller, "Scale effects in physical hydraulic engineering models," *J. Hydraul. Res.*, vol. 49, no. 3, pp. 293–306, 2011.

[53] Y. Zhiyin, "Large-eddy simulation: Past, present and the future," *Chinese J. Aeronaut.*, vol. 28, no. 1, pp. 11–24, 2015.

[54] I. ANSYS, "ANSYS Fluent 12.0 theory guide," *ANSYS FLUENT Release*, 2009.

[55] T. Salimans, I. Goodfellow, W. Zaremba, V. Cheung, A. Radford, and X. Chen, "Improved techniques for training gans," in *Advances in neural information processing systems*, 2016, pp. 2234–2242.

[56] M. S. Bazaraa, J. J. Jarvis, and H. D. Sherali, *Linear programming and network flows*. John Wiley & Sons, 2011.

[57] J. E. Pearson, "Comparison of scintillometer and microthermometer measurements of CN2," *JOSA*, vol. 65, no. 8, pp. 938–941, 1975.

[58] R. S. Lawrence, G. R. Ochs, and S. F. Clifford, "Measurements of atmospheric turbulence relevant to optical propagation," *JOSA*, vol. 60, no. 6, pp. 826–830, 1970.

[59] E. Masciadri and P. Jabouille, “Improvements in the optical turbulence parameterization for 3D simulations in a region around a telescope,” *Astron. Astrophys.*, vol. 376, no. 2, pp. 727–734, 2001.

[60] J. L. Caccia, M. Azouit, and J. Vernin, “Wind and CN2 profiling by single-star scintillation analysis,” *Appl. Opt.*, vol. 26, no. 7, pp. 1288–1294, 1987.

Vita

My name is Luis Fernando Rodriguez Sanchez and I am pursuing a doctoral degree in Mechanical Engineering at the University of Texas at El Paso under Dr. Vinod Kumar as my faculty advisor. Before starting my doctoral studies at UTEP, I practiced for ten years as professor of the Mechanical Engineering Department at the prestigious university Tec de Monterrey in Mexico. During this period, I had the opportunity to serve as director of the undergrad programs of Mechanical Engineering and Automotive Engineering.

Before starting my labor as a professor, I gained extensive experience for ten years in the fields of automotive and electronics manufacturing. In the automotive production lines, I focused above all in the redesign of structural systems such as the chassis' components of the Chrysler's heavy-duty trucks. As for the electronic production lines I focused on the implementation of new projects in the manufacturing lines of the company named Flextronics.

The experience gained in the industry as well as in the educational environment, allows me to be involved very strongly into the research projects because I have the knowledge of the productive branch as well as the one of the educational branch where it is possible to focus on a large number of projects that the industry requests from the universities.

Contact Information: fernando.rodriguez@live.com